Non-random segregation of sister chromosomes by *Escherichia coli* MukBEF axial cores

Jarno Mäkelä, Stephan Uphoff, David J. Sherratt

Department of Biochemistry, University of Oxford, Oxford OX1 3QU, UK
Correspondence to: jarno.makela@bioch.ox.ac.uk; david.sherratt@bioch.ox.ac.uk

Summary

The *Escherichia coli* structural maintenance of chromosomes complex, MukBEF, forms axial cores to chromosomes that determine their spatio-temporal organization. Here, we show that axial cores direct chromosome arms to opposite poles and generate the translational symmetry between newly replicated sister chromosomes. MatP, a replication terminus (*ter*) binding protein, prevents chromosome rotation in the longitudinal cell axis by displacing MukBEF from *ter*, thereby maintaining the linear shape of axial cores. During DNA replication, MukBEF-MatP action directs lagging strands towards the cell center, marked by accumulation of DNA-bound β_2-clamps in the wake of the replisome, in a process necessary for translational symmetry. Finally, the ancestral template DNA strand, propagated from previous generations, is preferentially inherited by the cell forming at the old pole, dependent on MukBEF-MatP. The work demonstrates how chromosome organization-segregation fosters non-random inheritance of genetic material and provides a framework for understanding how chromosome conformation and dynamics shape subcellular organization.

Highlights

- Linear MukBEF axial cores are required for *left-oriC-right* chromosome organization
- MatP prevents longitudinal nucleoid rotation by linearizing the axial cores
- MukBEF axial cores direct lagging strands towards the cell center
- The ancestral DNA strand is preferentially segregated to the older pole cell

Introduction

Faithful chromosome propagation and inheritance underpin all replicative life. Organisms have evolved a vast range of mechanisms to ensure timely replication and segregation of genetic material. Eukaryotic cells orchestrate replication and segregation in discrete stages where newly replicated sister chromosomes are first individualized by condensin and held together by cohesin before being pulled apart by action of the mitotic spindle and cleavage of cohesion (reviewed in (Uhlmann, 2016)). In prokaryotes, chromosomes replication and segregation are not temporally separated, limiting bacteria to a single replicon and segregon per chromosome (Kuzminov, 2014). Because divergent bacterial species have evolved different solutions to the same problem, understanding the contributions of different mechanisms and physical constraints underlying robust chromosome segregation remains a

challenge (Badrinarayanan et al., 2015; Surovtsev and Jacobs-Wagner, 2018; Wang et al., 2013).

Genetic studies have identified two major classes of proteins implicated in chromosome segregation in bacteria. First, structural maintenance of chromosomes (SMC) complexes, MukBEF, MksBEF and Smc-ScpAB; with MukBEF initially identified in a screen for *Escherichia coli* mutants that generated anucleate cells as a consequence of a failure to segregate newly replicated chromosomes to daughter cells (Hiraga et al., 1989; Nolivos and Sherratt, 2014). Second, studies of low copy plasmid stability identified ParAB*S* systems, which subsequently were shown to have roles in chromosome segregation in many organisms (Surovtsev and Jacobs-Wagner, 2018). While many bacteria encode one or both of these systems, some, for example *Pseudomonas aeruginosa*, encode two different SMCs and a ParAB*S* system (Petrushenko et al., 2011; Vallet-Gely and Boccard, 2013). Nevertheless, deletion of SMC or ParAB proteins has frequently modest if any consequences for chromosome segregation. Consistent with this, it has been proposed that large bacterial chromosomes can utilise repelling entropic effects to facilitate separation of bacterial chromosomes (Jun and Mulder, 2006), unlike much smaller low copy number plasmids that require a functional ParAB*S* system for faithful segregation (Surovtsev and Jacobs-Wagner, 2018). Whatever roles entropic forces may play, studies in diverse bacterial species have demonstrated that chromosomal loci are not positioned randomly in cells (Fogel and Waldor, 2005; Umbarger et al., 2011; Vallet-Gely and Boccard, 2013; Wang et al., 2005, 2006, 2014), and that in *E. coli*, MukBEF complexes play an important role in correct positioning of replication origins and other loci by forming an axial core to the chromosome (Danilova et al., 2007; Mäkelä and Sherratt, 2020). Absence of MukBEF leads to formation of anucleate cells during growth and loss of viability at temperatures higher than 22 °C in rich media (Danilova et al., 2007; Niki and Jaffe, 1991).

In new-born *E. coli* cells growing under conditions in which replication cycles do not overlap, origins of replication (*oriC*) are positioned close to the cell center, and the left and right chromosome arms are linearly organized in separate cell halves. Chromosome replication-segregation leads to generation of daughter cells with a chromosome organization identical to their mother cell. Most cell adopt a *left-oriC-right-left-oriC-right* (*L-R-L-R*) translational symmetry prior to division (Wang et al., 2006), which requires that either the leading or lagging strand templates are symmetrically segregated to the cell poles (Toro and Shapiro, 2010; Wang et al., 2005). In agreement, an elegant chromosome degradation experiment showed that the leading strand templates are segregated towards the cell poles in most cells (White et al., 2008). In theory, cells could also control the fate of the old template strand by non-random segregation, designating the destination for each strand. During each replication cycle, there is a risk of the new strand not faithfully copying the information from the template strand. 'Immortal' strand retention was originally proposed as a strategy to maintain DNA purity in stem cells while the copied strands, potentially carrying mutations from replication, were segregated to non-stem cell progeny (Cairns, 1975). Whether this strategy is actually utilized by stem cells remains controversial (Lansdorp, 2007; Rando, 2007; Wakeman et al., 2012). Ancestral strand segregation has also been tested in *C. crescentus* (Marczynski et al., 1990; Osley and Newton, 1974) and *B.*

subtilis (Errington and Wake, 1991), however, none of these studies showed any segregational strand preference between daughter cells.

We lack a mechanistic understanding of how chromosome conformation and orientation is maintained inside a bacterial cell. It also remains unknown how progressive chromosome segregation facilitates non-random sister chromosome inheritance in an otherwise apparently symmetrical organism. In this study, we address these questions in *E. coli* utilizing microfluidics time-lapse imaging, high-throughput microscopy and quantitative analysis. We first demonstrate that in the absence of MukBEF, anucleate cells arise predominantly from the mother cell's new pole as a consequence of the failure to segregate new replicated origins in a timely fashion. We show that newly replicated lagging strands and their templates are directed towards cell centers, a process that is required for the observed translational *L-R-L-R* segregational symmetry; and which is perturbed in the absence of MukBEF. Furthermore, we show directly that the ancestral DNA strand, inherited from previous generations, is preferentially segregated to the old cell pole dependent on both MukBEF and its partner MatP. Lack of MatP does not perturb immediate asymmetry after replication-segregation; rather it leads to loss of chromosome orientation during cell cycles, consistent with the observed loss of ancestral strand retention at old poles. Taken together, the results explain how MukBEF axial cores and their MatP-driven depletion from the *ter* region, lead to asymmetric strand and chromosome segregation. The possible functional and evolutionary consequences of this are explored.

Results

In the absence of MukBEF, anucleate cells arise from the newer mother cell pole

To understand how anucleate *E. coli* cells form in the absence of MukBEF, we followed successive cell cycles of *ΔmukB* cells with *oriC* and *ter* (*ori1* and *ter3*) regions fluorescently labeled by FROS markers. We used a 'mother machine' microfluidics device (Uphoff, 2018; Wang et al., 2010) to follow thousands of cell generations and identify changes in chromosome organization that correlate with chromosome mis-segregation. Under these conditions, 15.7 ± 0.4% (±SD) of divisions led to the formation of an anucleate daughter cell (Fig. 1A, Fig. S1).

In *ΔmukB* cells *ori1* was of often mis-localized towards the old pole at birth, rather than at midcell (Fig. 1B), as previously observed for wild type (WT) cells (Wang et al., 2006). As the cell cycle progressed, *ori1* localized preferentially towards the old cell pole, with newly replicated sister *ori1* loci frequently remaining in close proximity. In contrast, *ter3* migrated from the new-born cell pole to midcell similar to what has been previously reported (Fig. 1B)(Wang et al., 2005). ~80% of anucleate cells were generated when duplicated *ori1* loci in mother cells remained together in the region of the old pole prior to cell division (Fig. 1C). In contrast, in ~70% of mother cells where chromosome segregation was faithful, *ori1* loci were visible as separate foci (Fig. 1C). Delayed separation of newly replicated *ori1* loci could be a consequence of delayed decatenation, since the decatenase TopoIV, is no longer recruited by MukBEF to *oriC*-proximal regions (Zawadzki et al., 2015). Indeed, modest over-expression of TopoIV leads to a reduction in cohesion time of newly replicated *oriC* from ~14 min to ~5 min (Wang et al., 2008). In anucleate cell divisions,

128 daughter cells that inherited both chromosomes divided normally after a modest increase in
129 generation time (Fig. S1).
130 Prior to anucleate cell formation, mother cells divided nearly symmetrically (2.1 ± 0.2
131 µm and 2.4 ± 0.2 µm, respectively (±SD); two-sample t-test p-value 0.17), with the divisome
132 being placed close to midcell. While the average anucleate cell length at birth did not
133 significantly differ from that of the sister, the growing sister was systematically longer than
134 the anucleate sister (Fig. S1), the bias for the longer growing sister increasing with mother
135 cell division size. Importantly, we showed that anucleate cells formed preferentially at the
136 newer mother cell pole (74.4 ± 1.8% (±SD), Fig. 1D). Therefore, anucleate cell formation is
137 associated with the nucleoid being preferentially retained at the old pole of *ΔmukB* mother
138 cells, while in the case of WT cells the nucleoid is localized closer to the newer pole of the
139 dividing cell (Fisher et al., 2013). We conclude that mis-localization of *ori1* towards the old
140 pole, accompanied by delayed segregation of newly replicated *ori1* loci, directs the
141 formation of anucleate cells to the mother cell's new pole.
142
143 ***MukBEF and MatP direct left-oriC-right chromosome organization***
144 Next we investigated how MukBEF directs chromosome organization and segregation in
145 growing cells. MukBEF and MatP have been proposed to be major factors in dictating *left-*
146 *oriC-right* (*L-R*) chromosome organization in *E. coli.* MukBEF complexes form axial cores that
147 linearly organize the chromosome outside the 800 kb *ter* region, from where MatP bound to
148 *matS* sites displaces MukBEF (Fig. 2A)(Mäkelä and Sherratt, 2020). Complete axial cores
149 were most easily visualized in cells in which MukBEF occupancy on the chromosome was
150 increased ~3.5-fold, while cells with WT MukBEF abundance on chromosomes exhibited
151 more granular structures (Mäkelä and Sherratt, 2020). To characterize how MukBEF axial
152 cores influence chromosome organization during the cell cycle, we used strains that allowed
153 us to test the requirements for *left* and *right* chromosome arm organization in relation to
154 *oriC* and *ter* in MatP$^+$ and *ΔmatP* cells with WT levels of MukBEF, and in *ΔmukB* cells (Fig. 2).
155 The *left* and *right* chromosome arms were labeled at *L3* and *R3* (128° and 122° from *oriC*,
156 respectively) with FROS markers, as were *ori1* and *ter3* loci (Fig. 2A, B).
157 New-born WT cells exhibited the distinctive *left-oriC-right* (*L3-R3*) chromosome
158 organization (Fig. 2C, D and E, Fig. S2), where *oriC* remained at the cell center and the
159 chromosome arms (*L3* and *R3*) resided in opposite cell halves (97.8 ± 0.6% (±SD), Fig. 2F and
160 G) (Nielsen et al., 2006; Wang et al., 2006). During replication-segregation, the pattern was
161 extended into a translationally symmetric *left-oriC-right-left-oriC-right* (*L3-R3-L3-R3*) pattern
162 in 73.1 ± 3.9% (±SD) of WT cells (Fig. 2G). In the absence of MukBEF, we expected
163 chromosome organization to be more 'relaxed' as lengthwise chromosome compaction is
164 relieved (Mäkelä and Sherratt, 2020). Indeed, the localization of all four chromosomal
165 markers was less precise, with a wide distribution of *L3-R3* distances (Fig. 2F), fewer *L3* and
166 *R3* foci localized in opposite cell halves (56.6 ± 3.2% (±SD), Fig. 2G), and a random chance of
167 observing the *L3-R3-L3-R3* organization (47.7± 0.2% (±SD), versus *L3-R3-R3-L3* or *R3-L3-L3-*
168 *R3*. The impaired chromosome organization in *ΔmukB* cells is frequently accompanied by
169 the chromosome arms being aligned together along the long cell axis with *ori1* towards the
170 old cell pole (Fig. 2B and D)(Danilova et al., 2007), an organization reminiscent of the

171 situation in *C. crescentus* (Wang et al., 2013). We conclude that absence of lengthwise
172 compaction by MukBEF axial cores causes loss of both the distinctive *L-R* chromosome
173 organization prior to replication and the *L-R-L-R* organization after replication.
174 Absence of MatP leads to circular MukBEF axial core formation, rather than linear
175 ones (Fig. 2A). We observed that Δ*matP* cells exhibited chromosome locus localization
176 patterns strikingly different from that of WT and *ΔmukB* cells (Fig. 2 C and E). The average
177 distance between *L3* and *R3* was reduced two-fold (Fig. 2F), consistent with MukBEF-
178 mediated lengthwise compaction of *ter* in the absence of MatP (Mäkelä and Sherratt, 2020).
179 Lengthwise compaction of *ter* reduced the efficiency of *L3* and *R3* being directed into
180 opposite cell halves (65.7 ± 0.8% (±SD), Fig. 2G). Concomitantly, it also led to *L3* and *R3* foci
181 being preferentially localized closer to cell center than segregated sister *ori1* loci during
182 replication, in contrast to WT cells where *L3* and *R3* localize towards the cell poles (Fig. 2E).
183 Surprisingly, despite these substantial perturbations, the normal *L3-R3-L3-R3* organization
184 was retained in Δ*matP* cells prior to cell division (80.2 ± 1.9% (±SD)).
185 Because the circular MukBEF axial cores of Δ*matP* cells lead to rotational
186 chromosome symmetry (Mäkelä and Sherratt, 2020), we hypothesized that non-replicating
187 chromosomes in new born cells are free to rotate around the longitudinal axis of the cell.
188 This would switch the configuration from *L3-R3* to *R3-L3* (or *vice versa*); while bi-lobed
189 replication intermediates could prevent the rotation as replication progresses. To test this
190 hypothesis, we followed Δ*matP* cells under the microscope to observe how often the *L3-R3-*
191 *L3-R3* orientation flips to *R3-L3-R3-L3* (or *vice versa*) in consecutive generations (Fig. S2).
192 Indeed, *ΔmatP* cells retained the chromosome orientation only in 32.2 ± 4.6% (±SD) of
193 daughter cells, while WT cells predominantly retained the orientation (91.4 ± 5.2% (±SD),
194 Fig. 2H). We propose that the *L3-R3-L3-R3* organization arises from an interplay between
195 bidirectional replication and the action of MukBEF axial cores.
196
197 ***DnaN marks lagging strand segregation to the cell center***

198 Translational symmetry of sister chromosomes arises at least in part from the symmetric
199 segregation of lagging strands during DNA replication towards midcell (and leading strands
200 towards the cell poles) (White et al., 2008). While this work used an elegant genetic system
201 to infer the segregation pattern, we sought directly to visualise the positioning of lagging
202 strands in WT, *ΔmatP* and *ΔmukB* cells.
203 During replication, ~20 DNA-bound β_2-clamps, which ensure DNA polymerase III
204 processivity, accumulate on the lagging strand and its template because of a ~3 min
205 residence time before clamps are unloaded from completed Okazaki fragments (Fig. 3A)
206 (Moolman et al., 2014). We reasoned that since β_2-clamps could potentially cover >100kb of
207 newly replicated lagging strand DNA, they could serve as a marker to monitor lagging strand
208 segregation (Fig. 3B). As a reference, for the localization of replication forks, we imaged
209 fluorescent DNA polymerase III ε-subunits (DnaQ). Strikingly, while DnaN localized in the
210 vicinity of cell center, DnaQ foci were more spread towards cell poles (Fig. 3C). By directly
211 measuring the distance from each DnaQ focus to the closest DnaN focus, we found that 41.2
212 ± 5% (±SD) of DnaQ foci do not colocalize with DnaN foci during replication (Fig. 3D).
213 Differential location of bulk DnaN and replication forks was confirmed by measurement of

214 the distances from replicative helicase (DnaB) foci to their closest DnaN focus (47.1 ± 6.1%
215 (±SD) not colocalizing) (Fig. S3B, C). Since DnaN and DnaQ colocalize during early and late
216 replication, when sister replisomes are necessarily close together, we also show focus
217 localization in mid-replication cycle (Fig. 3E), when independently tracking replication forks
218 are more frequently spatially separate. The pattern of DnaQ foci that did not colocalize with
219 DnaN foci (Fig. S3F) underlines the conclusion that spatially separate sister replisomes in
220 different cell halves have a different cellular location from the bulk DnaN. Our results are
221 consistent with previous independent measurements of DnaQ and DnaN localization, and
222 the observation that DnaN foci often do not spatially separate (Mangiameli et al., 2017;
223 Reyes-Lamothe et al., 2008; Wallden et al., 2016). They provide the first evidence that the
224 replisome and β_2-clamps frequently do not colocalize during replication.
225 Our direct visualization of the segregation of lagging strands during replication by
226 imaging DnaN, supports the previously shown symmetric segregation of leading strands
227 towards the cell poles (White et al., 2008). To analyze how MukBEF and MatP contribute to
228 lagging strand segregation, we measured DnaN localization in *ΔmatP* and *ΔmukB* cells. The
229 DnaN distribution in *ΔmatP* cells was much broader than in WT cells (Fig. 3E and F),
230 indicative of spatially less precise lagging strand segregation, but still directed towards cell
231 centers, as predicted by the *L3-R3-L3-R3* organization. The DnaQ distribution in mid-cycle
232 *ΔmatP* cells was more central than that of DnaN (Fig. 3E, 50.8 ± 1.3% (±SD) colocalization
233 with DnaN), most likely because of less separated chromosome arms. Both DnaQ and DnaN
234 exhibited a broader distribution at shorter cell lengths (Fig. 3F), presumably because of a
235 more random chromosome conformation (Fig. 2). *ΔmukB* cells exhibited a bimodal
236 distribution of DnaN and DnaQ localizations towards cell poles, with the DnaQ and DnaN
237 profiles being almost identical (Fig. 3G). This shows that lagging strands and their templates
238 cannot be directed to cell centers in a timely manner in the absence of MukBEF function, a
239 result consistent with impaired *L-R* and *L-R-L-R* organization in Δ*mukB* cells. By measuring
240 the distance from each DnaQ focus to the closest DnaN focus, we found that lagging strands
241 did not leave the vicinity of the replisome during the DnaN dwell time on chromosomes of
242 ~3 min (78.4 ± 0.5% (±SD) of foci; Fig. S3G). We hypothesize that this is a consequence of
243 delayed decatenation by TopoIV in the absence of MukBEF (Zawadzki et al., 2015), since
244 lagging strand templates can only be segregated from the leading strands once
245 decatenation has occurred.
246 Finally, a dynamin-like protein CrfC (aka YjdA) has been proposed to bind β_2-clamps
247 and tether the nascent strands of sister-chromosomes together (Ozaki et al., 2013).
248 However, upon deletion of *crfC*, we observed no changes to DnaN localization along the
249 long cell axis, or any decrease in the frequency of the *L3-R3-L3-R3* configuration (Fig. S3G,
250 H). This result indicates that CrfC is not necessary for WT chromosome conformation and
251 segregation.
252
253 ***Ancestral DNA strands are preferentially retained at older cell poles***
254 Previously it has been hypothesized that a symmetrical segregation of lagging strands to the
255 cell center leads to sister chromosomes‘ translational symmetry and, in consequence, the
256 ancestral template DNA strand is not randomly segregated to daughter cells over

257 subsequent generations (discussed in (Toro and Shapiro, 2010)). To address this theory, we
258 have developed a novel pulse-chase assay. It allowed us to visualize relative age of DNA
259 strands between sister chromosomes and relate their position to the older pole in individual
260 cells without the need for cell synchronization or tracking (Fig. 4A).
261 The assay comprises pulse labelling of newly replicated DNA and identifying relative
262 pole age by chemoreceptor accumulation at cell poles. The newly synthesized DNA was
263 labelled by a 15 min EdU (5-Ethynyl-2'-deoxyuridine) pulse, after which cells were washed,
264 and allowed to grow for 3 h (generation time ~150 min). To avoid EdU-mediated growth
265 defects, thymidine was added to the medium to outcompete EdU. We observed no
266 detrimental effects on growth rate or cell size from the low concentration of EdU used in
267 the pulse (Fig. S4). After the growth period, which was longer than a single generation time,
268 most cells have completed an additional round of replication resulting in only one of the
269 two sister chromosomes remaining EdU-labelled (Fig. 4A). Cells were fixed and EdU was
270 visualized by click-chemistry using Alexa 488 azide. In cells with segregated chromosomes
271 just before division, the chromosome with new strand was fluorescently labeled, while the
272 one with the ancestral strand was not.
273 To identify the older cell pole, we exploited the fact that the serine chemoreceptor,
274 Tsr, accumulates near-linearly with time at the cell poles. Hence the older pole can be
275 distinguished from the new pole by a higher quantity of fluorescently labeled Tsr (Ping et al.,
276 2008). A functional HaloTag fusion of the endogenous *tsr* gene was labeled with TMR dye,
277 and nucleoids were stained by DAPI (Fig. 4B). This allowed us to determine if the older
278 strand chromosome was segregated towards older or newer pole in each cell (Fig. 4C). We
279 limited analysis only to cells with segregated chromosomes (i.e. two visibly separate
280 nucleoid regions) only one of which displayed EdU fluorescence. This does not bias the
281 analysis towards a specific pole. In a time-lapse control experiment we confirmed that Tsr-
282 mYpet forms higher intensity foci at the older pole in 99.2 ± 0.5% (±SD) of cells.
283 We observed that 71.3 ± 3.9% (±SD) of WT cells contained EdU foci in the
284 chromosome closer to the new pole (Fig. 5A). Because EdU was incorporated into the new
285 template strand, this indicates that the ancestral strand is preferentially retained at the
286 older pole. The result deviates significantly from random retention, where the older pole
287 would have a 50% chance of inheriting either strand (binomial two-tailed test p-value < 10^{-}
288 ^{5}). We also compared the dispersion (SD) of our data to a binomial distribution with
289 different sample sizes to estimate reliability of our experiment (Fig. 5B). We found excellent
290 agreement showing that our measurements are robust for the given sample size, with no
291 additional noise sources, and increasing sample size would give diminishing returns.
292 How is ancestral strand retention related to chromosome organization? For this, we
293 tested the contributions of MukBEF and MatP to ancestral strand retention. Upon deletion
294 of *mukB*, we observed a random segregation of the ancestral strand (48.5 ± 3.8% (±SD), Fig.
295 5A), indicating a clear requirement for functional MukBEF for ancestral strand retention at
296 older poles. Deletion of *matP* also abolished the preferential segregation of the ancestral
297 strand (46.2 ± 1.1% (±SD), Fig. 5A). While MatP has not been implicated in early
298 chromosome segregation, when the segregation pattern(s) emerge, the influence of MatP
299 on MukBEF action is crucial as it prevents longitudinal chromosome rotation (Fig. 2H), which
300 would disrupt ancestral-strand-older-pole association. MatP-*matS* also interacts with the

301 divisome through ZapB and this interaction has been proposed to partially anchor *ter* to the
302 inner cell membrane (Espéli et al., 2012). This interaction could plausibly contribute to the
303 ancestral strand retention by anchoring the chromosome and thereby preventing
304 chromosome rotation. However, upon replacing the native *matP* with a non-divisome
305 interacting *matPΔC20* mutant or deleting *zapB*, we did not observe any difference to WT
306 with regard to ancestral strand retention (71.0 ± 3.1% and 71.8 ± 1.0%, respectively (±SD);
307 Fig. 5A). This confirms that the loss of ancestral strand retention in *ΔmatP* cells is related to
308 the proposed longitudinal rotation of the chromosome over generations.
309 Finally, since MukBEF and MatP have co-evolved with a group of proteins (including
310 Dam and SeqA) that are related to Dam DNA methyltransferase activity (Brézellec et al.,
311 2006), we tested the influence of these proteins in the ancestral strand retention. Dam
312 methylates adenines in the sequence GATC, which transiently distinguishes strands after
313 replication because of delayed methylation of the newly replicated strands. Prior to Dam
314 methylation, SeqA binds to hemimethylated GATC sites, negatively regulating replication
315 initiation and possibly contributing to chromosome segregation (reviewed in
316 (Waldminghaus and Skarstad, 2009)). Deletion of either *dam* or *seqA* did not influence
317 ancestral strand retention at older poles (69.9 ± 1.5% and 67.6 ± 3.3%, respectively (±SD);
318 Fig. 5A), indicating GATC methylation patterns do not affect the observed asymmetry and
319 consequently, overall *L-R* chromosome organization.
320
321 **Discussion**

322 Our results demonstrate how MukBEF axial cores direct nucleoid organization and non-
323 random segregation of sister chromosomes in *E. coli*. This work extends that describing
324 chromosome organization by MukBEF axial cores (Mäkelä and Sherratt, 2020), and uncovers
325 important principles of nucleoid organization and replication-segregation. The main features
326 of nucleoid organization are illustrated in Fig. 6 and outlined below.
327
328 1. MukBEF axial cores, linearized by *matS*-MatP-mediated depletion of MukBEF from
329 *ter*, are required for *left-oriC-right* chromosome locus organization along the long
330 cell axis.
331 2. The linearity of axial cores prevents longitudinal nucleoid rotation, thereby retaining
332 the *left-oriC-right* chromosome orientation over generations.
333 3. Translational symmetry of the sister chromosomes results from the interplay of axial
334 cores and segregation of lagging strand towards the cell center.
335 4. The ancestral DNA strand is preferentially segregated to the older pole cell over
336 generations, a process dependent on MukBEF and MatP.
337 5. Absence of MukBEF leads to anucleate cell formation predominantly at the newer
338 mother cell pole, largely because of failure to segregate newly replicated origins
339 from the vicinity of the older pole.
340
341 Our analyses provide molecular mechanisms underlying the *E. coli* chromosome
342 organization and segregation, and complement previous studies that have rigorously
343 quantified the nucleoid dynamics in mechanical terms (Cass et al., 2016; Fisher et al., 2013;

344 Fritsche et al., 2012). The model succinctly explains previous observations and provide a
345 conceptual foundation for understanding how nucleoid conformation and dynamics shape
346 the subcellular organization.
347
348 ***E. coli chromosome organization***

349 Stiff nucleoid 'bundles' that are radially confined by cell dimensions and exhibit a contour
350 length of the scale of cell dimensions were characterized in live-imaging studies of WT *E. coli*
351 (Fisher et al., 2013). Bundles were also identified in cells with increased volume, which
352 allowed visualisation of non-replicating toroidal chromosomes (Wu et al., 2019). We
353 propose that MukBEF axial cores correspond to these bundles; the duality of the bundles
354 observed in WT cells likely relate to the bimodal nature of axial cores in non-replicating
355 MatP$^+$ cells. We hypothesize that individual dimer of dimer MukBEF complexes within axial
356 cores form DNA loops using energy from ATP, most likely through progressive loop
357 enlargement (Davidson et al., 2019; Ganji et al., 2018; Goloborodko et al., 2016). Unloading
358 and re-loading of MukBEF complexes will impact nucleoid spatio-temporal dynamics and
359 could be dependent on intra-chromosomal stress (Fisher et al., 2013). The correlative
360 timescale of bundle dynamics is of the order of a minute, similar to the dwell time of
361 individual MukBEF complexes on the chromosome (Badrinarayanan et al., 2012; Fisher et
362 al., 2013; Mäkelä and Sherratt, 2020). MukBEF forms a linear axial core to the chromosome
363 by compacting the chromosome lengthwise outside of *ter*, where *matS* bound MatP
364 displaces MukBEF (Mäkelä and Sherratt, 2020). The absence of MatP leads to formation of
365 circular symmetric MukBEF axial cores. Theoretical studies concluded that lengthwise
366 compaction of the chromosome (by MukBEF) would maintain the linear organization and
367 forms rigid chromosome bundles (Marko and Siggia, 1997). We propose that the linearity of
368 the axial core reduces the dimensions of free chromosome movement, thereby preventing
369 longitudinal chromosome rotation and therefore explaining how chromosome loci can be
370 robustly positioned along the long cell axis in a colinear manner outside of *ter* (Fig. 6).
371 Previous attempts to explain chromosome locus positioning by a randomly oriented
372 polymer, or by transcription factor-mediated DNA loops fail to explain nucleoid organization
373 in Δ*mukB* or Δ*matP* cells (Fritsche et al., 2012; Jun and Mulder, 2006). The presence of
374 MukBEF axial cores explains how loss of a flexible *ter* region in the absence of MatP results
375 in chromosome arms being closer together, as shown here. A flexible *ter* region might be
376 required for efficient chromosome segregation during fast growth as Δ*matP* cells exhibit
377 more frequent anucleate cell production than MatP$^+$ cells (Mercier et al., 2008). Broadly, we
378 propose that the rigid linear axial core removes the requirement for membrane anchoring
379 to orient and/or position the chromosome and could be a requirement for robust
380 segregation during overlapping replication cycles. Membrane tethering is generally found in
381 organisms in which MukBEF has been replaced by Smc-ScpAB complexes and which carry a
382 *parABS* segregation system; e.g. through PopZ in *C. crescentus* (Ebersbach et al., 2008),
383 HubP in *V. cholera* (Yamaichi et al., 2012), and RacA/DivIVA in sporulating *B. subtilis* (Ben-
384 Yehuda et al., 2003; Wu and Errington, 2003). Membrane anchoring typically uses ParB
385 bound to *oriC*-proximal *parS* sites as an intermediary. Intriguingly, some bacteria, such as *V.*
386 *cholera* or *P. aeruginosa*, not only encode MukBEF/MksBEF, but also specify a *parABS*

387 system (David et al., 2014; Vallet-Gely and Boccard, 2013). Whether organisms that encode
388 MukBEF orthologs, but not typical Smc-ScpAB complexes, and which lack ParABS systems,
389 generally have life cycles that encompass overlapping replication cycles, similar to *E. coli*,
390 remains to be determined.
391
392 ***Sister chromosome replication and segregation***

393 Chromosome organization specified by the MukBEF axial core directs the translational
394 symmetric (*L-R-L-R*) segregation of sister chromosomes during replication (Fig. 6), which
395 alone is insufficient for this organization (Fig. 6). Lengthwise compaction of newly replicated
396 DNA promotes individualization of sister chromosomes through excluded volume
397 interactions and by maximization of conformational entropy that leads to repulsion
398 between sister chromosomes (Goloborodko et al., 2016; Marko and Siggia, 1997). The
399 presence of the *L-R-L-R* segregation pattern of sister chromosomes in both WT and Δ*matP*
400 cells indicates that the pre-replication organization of the chromosome, where chromosome
401 arms are directed into separate cell halves only in WT cells, is not required for establishing
402 this pattern. While symmetrically lengthwise compacted chromosomes in Δ*matP* cells (Fig.
403 2A)(Mäkelä and Sherratt, 2020) are prone to change *L-R* orientation in non-replicating cells,
404 bi-loped replication intermediates prevent rotation during late replication (Fig. 6).
405 The relationship between *L-R-L-R* chromosome organization and symmetrical
406 segregation of leading/lagging strands has been discussed previously in relation to the
407 observed leading strand spatial segregation pattern (Toro and Shapiro, 2010; White et al.,
408 2008). Consistent with this, we observed accumulation of β_2-clamps, present primarily on
409 lagging strands, towards cell centers of replicating cells, when compared to both DNA
410 polymerase III and helicase localization. Differential positioning of the replisome and β_2
411 clamps resolves the conundrum that emerged from studies that favoured a model of a
412 single replication 'factory' containing two replisomes, based on clamp labelling (Mangiameli
413 et al., 2017). The results support the model of independent tracking of the two often
414 spatially separated replisomes in cells undergoing a single round of replication (Japaridze et
415 al., 2020; Reyes-Lamothe et al., 2008). A dynamin-like protein YjdA (aka CrfC), a possible
416 candidate for directing β_2-clamps to the cell centre, was not required for this action.
417 Because clamp localization at the cell center is dependent on the formation of linear axial
418 cores, we hypothesize that MukBEF could plausibly differentiate the strands, e.g. leaving
419 lagging strands less compacted (Fig. 6). However, the different contributions of MukBEF
420 activity are difficult to delineate, as in the absence of MukBEF, cohesion time is increased
421 and *L-R* organization prior to replication is impaired (Fig. 1).
422 Our results also show that the lifetime of individual chromosome-associated clamps
423 (estimated to be ~3 min (Moolman et al., 2014)) must be longer than the daughter
424 chromosome cohesion time for chromosomal regions outside of *oriC* and *ter* (estimated ~14
425 min and ~9 min, respectively) (Nolivos et al., 2016; Wang et al., 2008). Cohesion time is
426 largely determined by the time required for TopoIV to remove replicative catenanes
427 (Nolivos et al., 2016; Wang et al., 2008; Zawadzki et al., 2015). In addition, slower *oriC*
428 segregation may additionally require accumulation of sufficient newly replicated DNA that
429 leads to abrupt separation of newly replicated sister chromosomes (Cass et al., 2016; Fisher

et al., 2013). Cohesion time is influenced by the absence of MukBEF, which promotes TopoIV activity (Nolivos et al., 2016; Zawadzki et al., 2015), although tethering of *ter* to the divisome through MatP-ZapB interactions may also influence cohesion time in this region (Monterroso et al., 2019). Precise measurements of cohesion times for the rest of the chromosome have been refractory to precise experimental determination.

Ancestral strand retention at the older pole

We have directly shown preferential ancestral strand retention towards the older poles in *E. coli* orchestrated by the translational symmetry of the sister chromosomes (*L-R-L-R*), along with efficient maintenance of chromosome orientation over generations. Intriguingly, loss of preferential segregation in the absence of MukBEF is correlated with longitudinal *oriC-ter* chromosome organization along the long cell axis where chromosome arms are co-aligned, similar to *C. crescentus* and sporulating *B. subtilis*. However, as *E. coli* lacks the properties of cell differentiation, development and regeneration of a multicellular organism, it is not clear why it has evolved a chromosome organization that preferentially segregates the ancestral DNA strand to the older pole cell. *E. coli* older pole containing cells exhibit a constant growth rate for hundreds of generations (Wang et al., 2010). However, the death rate was found to increase with replicative cell age, which was attributed to growth-independent accumulation of protein damage (Wang et al., 2010). Increasing cellular maintenance processes through the general stress response reduced the death rate while its absence increased it (Yang et al., 2019). The older pole accumulates more membrane proteins (e.g. chemoreceptors, efflux pumps) than the new pole and in fluctuating or poor environment, these can significantly contribute to cell growth (Bergmiller et al., 2017; Ping et al., 2008). For example, the main multidrug efflux pump of *E. coli*, AcrAB-TolC, exhibits a strong partitioning bias for the older cell poles (Bergmiller et al., 2017). Consequently, older pole cells display increased efflux activity relative to new cell pole daughters giving the older pole cell a growth advantage under subinhibitory antibiotic concentrations and possibly protection against other toxic compounds. AcrAB-TolC pump activity is also required for acquiring a resistance gene from mobile genetic elements in the presence of antibiotics, as it reduces antibiotics concentrations inside the cell (Nolivos et al., 2019). Ancestral strand retention at older pole cells could therefore be beneficial to structured growth of *E. coli* in colonies where younger bacteria progress to a new terrain while the older ones stay closer to the colony center. Finally, older strand retention could simply be an evolutionary by-product of the *left-oriC-right* chromosome organization where chromosome orientation is retained. Nevertheless, since ancestral strand retention occurs in only ~70% of older-pole cells, this gives opportunities for selection in fluctuating or harmful environments independent of whether older or newer cell pole cells thrive better.

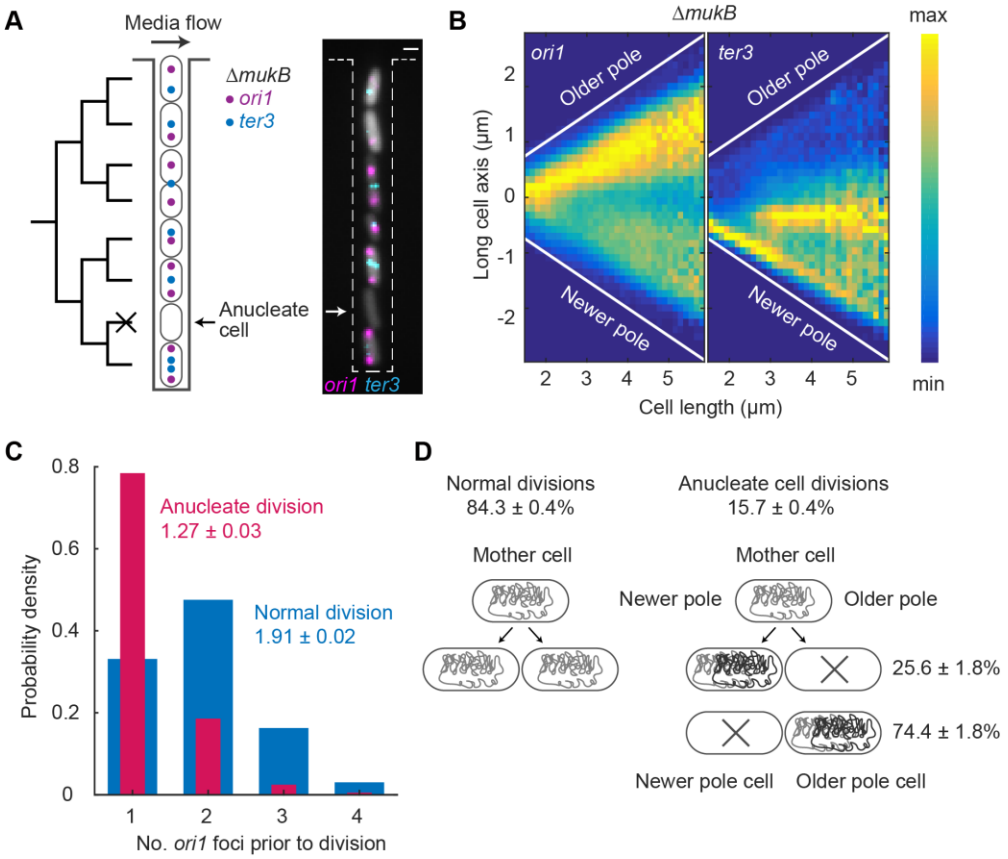

Fig. 1. Anucleate cell formation in absence of MukB is biased towards mother cell newer poles (**A**) Schematic of mother machine microfluidics device and representative cells in a channel. *ΔmukB* cells contain *ori1* and *ter3* FROS markers and a segmentation marker (grey). A non-growing anucleate cell lacking FROS markers is indicated. Scale bar: 1 µm. (**B**) *ori1* and *ter3* localization as a function of cell length in *ΔmukB* cells. Sample numbers with different cell lengths are normalized. 221057 cells. (**C**) Number of *ori1* foci prior to anucleate (one of the daughters is anucleate; 2444 cells) and normal cell division (10468 cells). Two-sample t-test between mean *ori1* numbers prior to anucleate and normal division p-value < 10^{-5}. (**D**) Percentage of anucleate cells forming at a mother cell's old and newer poles (2269 divisions). Percentage of anucleate cell divisions also shown (14392 divisions). All data from 3 repeats.

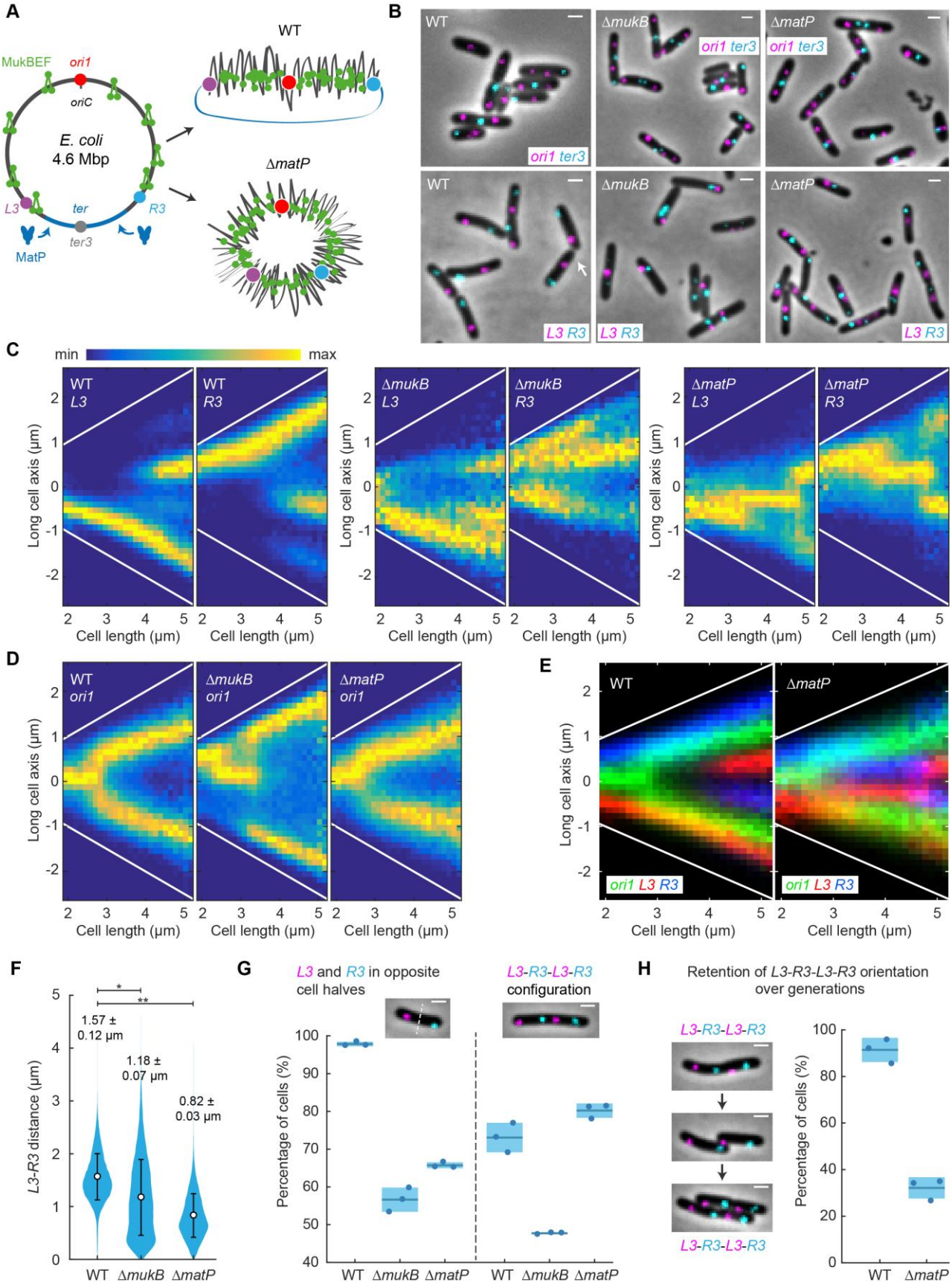
A
MukBEF
ori1
oriC
E. coli
4.6 Mbp
L3
ter
R3
ter3
MatP
WT
ΔmatP
B
WT
ΔmukB
ΔmatP
ori1 ter3
L3 R3
C
min
max
WT L3
WT R3
ΔmukB L3
ΔmukB R3
ΔmatP L3
ΔmatP R3
Long cell axis (μm)
Cell length (μm)
D
WT ori1
ΔmukB ori1
ΔmatP ori1
E
ori1 L3 R3
F
1.57 ± 0.12 μm
1.18 ± 0.07 μm
0.82 ± 0.03 μm
L3-R3 distance (μm)
G
L3 and R3 in opposite cell halves
L3-R3-L3-R3 configuration
Percentage of cells (%)
H
Retention of L3-R3-L3-R3 orientation over generations

482 **Fig. 2. MukBEF and MatP action generates and retains *left-oriC-right E. coli* chromosome**
483 **organization.** (**A**) *E. coli* chromosome circular map with *ori1*, *ter3*, *L3*, and *R3* loci illustrates
484 uniform MukBEF occupancy except for 800 kbp *ter*, from which *matS* bound MatP displaces
485 MukBEF. A folded chromosome conformation by linear MukBEF axial cores is shown with
486 and without MatP (for more details see (Mäkelä and Sherratt, 2020). (**B**) Representative
487 images of WT, *ΔmukB* and *ΔmatP* cells with *ori1* and *ter3*, or *L3* and *R3* FROS markers. Note
488 an atypical *R3-L3-L3-R3* configuration in WT (white arrow) in comparison to standard *L3-R3-*
489 *L3-R3*. Scale bars: 1 µm. (**C**) *L3* and *R3* localizations and (**D**) *ori1* localizations along the long
490 cell axis as a function of cell length in WT (*L3-R3* 57509 cells, *ori1* 42612 cells), *ΔmukB* (*L3-R3*
491 27984 cells, *ori1* 54820 cells) and *ΔmatP* (*L3-R3* 46679 cells, *ori1* 51350 cells). Sample
492 numbers with different cell lengths are normalized. Cells are oriented to place *L3* more
493 towards the negative pole (towards figure bottom) or, in the *ori1* data, *ter3* is oriented more
494 towards the negative pole (see Fig. S2). White lines denote cell borders. (**E**) Overlay of *ori1*
495 and *L3-R3* localization data in WT and *ΔmatP* from (C) and (D). (**F**) Distance between *L3* and
496 *R3* markers in WT (47376 cells), *ΔmukB* (15615 cells) and *ΔmatP* (41625 cells) in single *L3*
497 and *R3* focus cells. Mean and dispersion (SD) between cells are shown for each distribution.
498 * and ** denote two-sample t-test of *L3-R3* distances between WT and *ΔmukB* (p-value
499 0.0081) and WT and *ΔmatP* (p-value 5×10^{-4}), respectively. (**G**) (left) Percentage of cells with
500 *L3* and *R3* in opposite cell halves in single *L3* and *R3* focus cells (WT 47376 cells, *ΔmukB*
501 15615 cells, *ΔmatP* 41625 cells). (right) Percentage of cells with *L3-R3-L3-R3* (or *R3-L3-R3-L3*)
502 configuration (versus *L3-R3-R3-L3* or *R3-L3-L3-R3*) in double *L3* and *R3* focus cells (WT 10352
503 cells, *ΔmukB* 2535 cells, *ΔmatP* 6297 cells). Scale bars: 1 µm. (**H**) Percentage of cells
504 retaining *L3-R3-L3-R3* orientation (versus flipping to *R3-L3-R3-L3*) from a mother cell to a
505 daughter cell in WT (859 pairs) and *ΔmatP* (1054 pairs). Scale bars: 1 µm. Data from 3
506 repeats of each experiment.

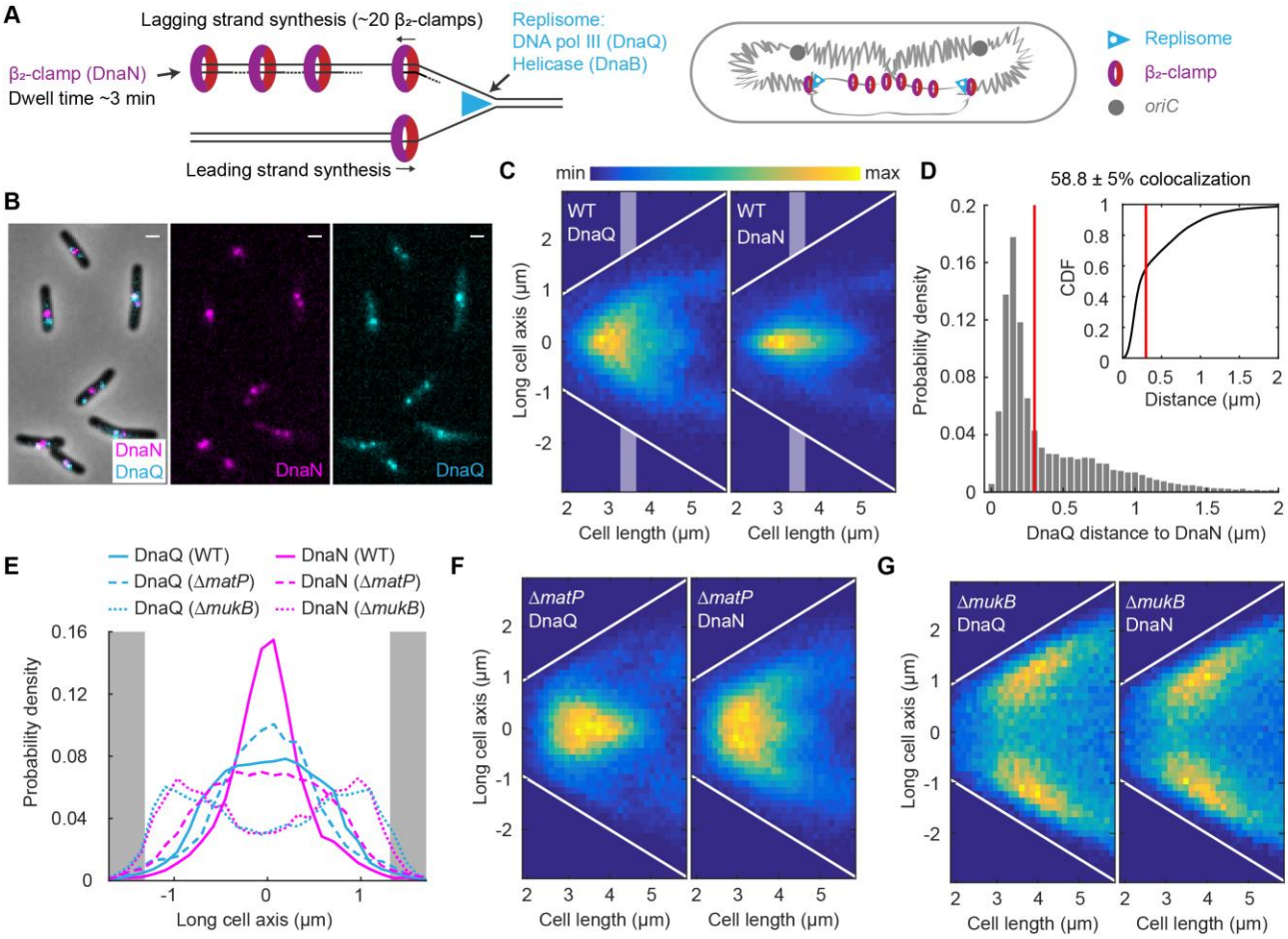

Fig. 3. DnaN visualizes the lagging strands during replication. (**A**) Schematic of accumulation of β_2-clamps (DnaN) on the lagging strand and its template during replication (Moolman et al., 2014). The DNA polymerase ε-subunit (DnaQ) marks the location of the replisome. (**B**) Representative images of WT cells with fluorescently labeled DnaN and DnaQ. Scale bars: 1 µm. (**C**) DnaQ and DnaN localization in WT cells as a function of cell length (37720 cells). White lines denote cell borders. Shaded areas denote intermediate cell lengths for localization data in (E). (**D**) Distance from a DnaQ focus to the closest DnaN focus. DnaQ and DnaN colocalize in 58.8 ± 5% (±SD) of focus pairs (38855 pairs) as defined by a threshold (red lines) below which two proteins colocalize (dictated by a diffraction limit of 300 nm). Inset shows the same data as a cumulative distribution. Same data as in (C). (**E**) DnaQ or DnaN localization with intermediate cell lengths (3.3-3.7 µm) in WT (DnaN 7104, DnaQ 8006 spots), *ΔmatP* (DnaN 11925, DnaQ 8025 spots) and *ΔmukB* (DnaN 5060, DnaQ 4205 spots) cells (see C, F, G). Full width at half maximum (FWHM) (±SD) of the distribution in WT: DnaN 0.67 ± 0.06 µm, DnaQ 1.67 ± 0.08 µm; and in *ΔmatP*: DnaN 1.85 ± 0.04 µm, DnaQ 1.14 ± 0.14 µm. Grey areas denote cell poles. (**F**) DnaQ and DnaN localization in *ΔmatP* cells (51956 cells) and in (**G**) *ΔmukB* cells (22902 cells) as a function of cell length. White lines denote cell borders. Data from 3 repeats in all analyses.

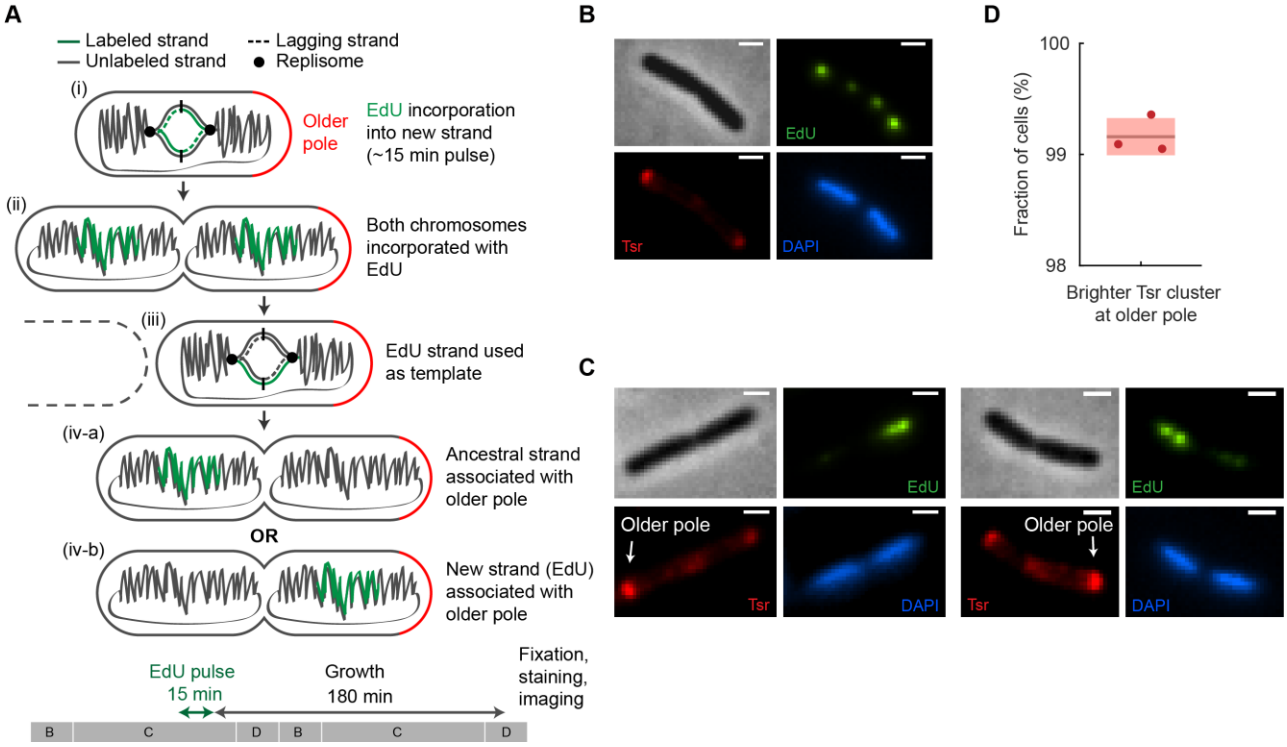

Fig. 4. Visualization of ancestral DNA strand retention in *E. coli*. (**A**) Ancestral DNA strand retention following an EdU pulse and the subsequent growth shown with cell cycle stages. After the 2nd round of replication only one of the chromosomes inherits the EdU label. Note that only a part of the chromosome is labelled with EdU. The 15 min EdU pulse and growth period are also shown relative to a schematic of cell cycle stages (B, C and D periods, generation time ~150 min). (**B**) Representative $EdU^{Alexa488}$, Tsr^{TMR} and DAPI images of a cell at stage (ii) (see (A)) after the EdU pulse. Note that each chromosome has two EdU foci because pulse-labeled chromosome arms are separated. Scale bars: 1 µm (**C**) Representative $EdU^{Alexa488}$, Tsr^{TMR} and DAPI images after the complete pulse-chase protocol (stage (iv), see (A)). The older pole is indicated with an arrow. Scale bars: 1 µm. (**D**) Accuracy of the older pole classification using Tsr prior to cell division. Shaded areas denote SD. Data from 2505 cells and 3 repeats.

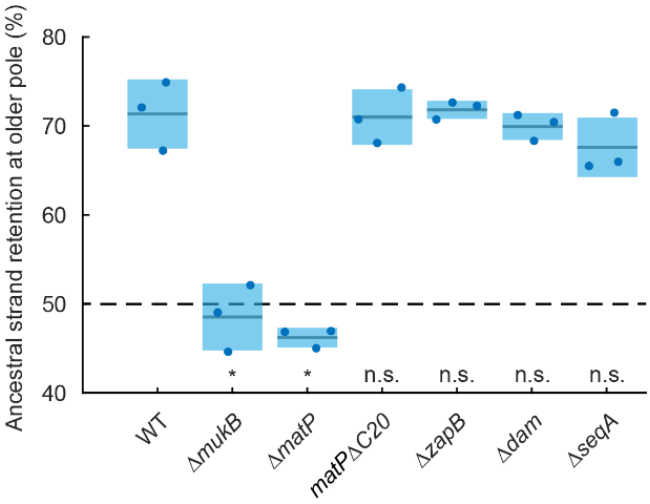

Fig. 5. Preferential retention of the ancestral strand at older cell poles requires functional MukBEF and MatP. Percentage of ancestral strands retained at the older pole in WT (988 cells), *ΔmukB* (427 cells), *ΔmatP* (1050 cells), non-divisome interacting *matPΔC20* mutant (1617 cells), *ΔzapB* (969 cells), *Δdam* (717 cells) and *ΔseqA* (473 cells). Dashed line shows random retention. p-value from two-proportion two-tailed z-test was used to test if binomial distributions significantly differ from WT; indicated by n.s. (> 0.01, non-significant) and * (< 0.01, significant) (p-values $<10^{-5}$, $<10^{-5}$, 0.51, 0.83, 0.26, and 0.03, respectively). Shaded areas denote SD. Data from 3 repeats.

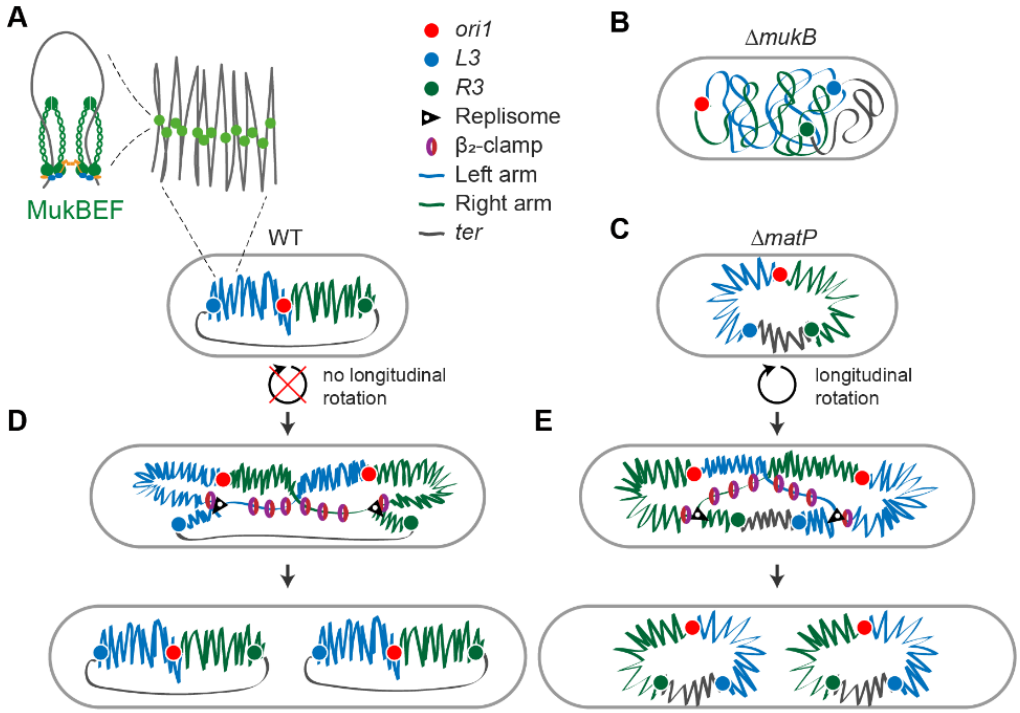

Fig. 6. Chromosome organization and segregation by MukBEF and MatP. (**A**) MukBEF dimer of dimer complexes form DNA loops dependent on ATP hydrolysis. Ubiquitous loop formation outside of *ter* compacts the chromosome lengthwise forming a linear axial core to the chromosome. Axial cores form stiff linear nucleoid bundles that localize chromosomal loci linearly along the long cell axis and maintain chromosome orientation by preventing longitudinal cell axis rotation. (**B**) Absence of functional MukBEF increases the effective contour length of chromosomes, leading to mis-localization of chromosome loci and loss of *left-oriC-right* organization of the chromosome. (**C**) MukBEF forms a complete circular axial core to the chromosome in the absence of MatP. Consequently, chromosome arms cannot be efficiently directed to opposite cell halves, *left-oriC-right* organization in non-replicating cells is impaired and chromosomes rotate in the longitudinal cell axis. During replication and prior to division, WT (**D**) and *ΔmatP* cells (**E**) exhibit translational symmetric (*L-R-L-R*) segregation of sister chromosomes. This is accompanied by the symmetric segregation of lagging strands and their templates during replication, as visualized by accumulation of β_2-clamps. Relative FROS marker, replisome and β_2-clamps localizations are derived from the data generated here.

571 **Methods**

572 **Bacterial strains and growth conditions**

573 Bacterial strains and primers are listed in Table S1 and S2, respectively. All strains were
574 derivatives of *E. coli* K12 AB1157 (Bachmann, 1996). *kan*, *cat*, *gen*, and *hyg* refer to insertions
575 conferring resistance to kanamycin (Km^r), chloramphenicol (Cm^r), gentamycin (Gm^r) and
576 hygromycin B (Hyg^r), respectively. The insertions are flanked by Flp site-specific
577 recombination sites (*frt*) that allow removing the resistance gene using Flp recombinase from
578 plasmid pCP20 (Datsenko and Wanner, 2000). *tsr-HaloTag-kan* and *tsr-mYpet-kan* were
579 inserted into the native *tsr* chromosomal locus using λ-red recombination (Datsenko and
580 Wanner, 2000). The generated gene loci were transferred by phage P1 transduction to
581 AB1157 yielding strains JM122 (*tsr-HaloTag-kan*) and JM133 (*tsr-mYpet-kan*). Deletion strains
582 of JM122 were constructed by P1 transduction, first removing the *kan* resistance gene using
583 Flp recombinase. *L3-R3* deletion strains were constructed from RRL66 using P1 transduction.
584 The microfluidics strain (JM09) was constructed from RRL189 by introducing *Δflhd-kan* and
585 *ΔmukB-kan* by consecutive rounds of P1 transduction and Flp recombination. GFPmut2 cell
586 marker was inserted at an *attTn7* site by a plasmid transformation as described in (McKenzie
587 and Craig, 2006). The DnaQ and DnaN labeled strain (JM141) was constructed from RRL388
588 using P1 transduction from RRL36. Deletion strains of JM141 were constructed by P1
589 transduction, first removing the *kan* resistance gene using Flp recombinase. JM142 and
590 JM143 were constructed by P1 transduction from JW4070. All genetic modifications were
591 verified by PCR and/or sequencing and behavior in quantitative imaging. *mukB* deletions were
592 verified by temperature-sensitivity in rich media, as described in (Nolivos et al., 2016).

593 Cells were grown in M9 minimal medium supplemented with 0.2% (v/v) glycerol, 2 μg
594 ml^{-1} thiamine, and required amino acids (threonine, leucine, proline, histidine and arginine;
595 0.1 mg ml^{-1}) at 30 °C. For microscopy, cells were grown overnight, diluted 1000-fold and
596 grown to an A_{600} of ~0.1. Cells were then pelleted, spotted onto an M9 glycerol 1% (w/v)
597 agarose pad on a slide and covered by a coverslip. In mother machine microfluidics
598 experiments, cells were first grown in M9 minimal medium with 0.2% (v/v) glycerol at 30 °C
599 (as above), and then placed inside the microfluidics device, when the media was changed to
600 M9 minimal medium supplemented with 0.2% (v/v) glucose, 2 μg ml^{-1} thiamine, MEM amino
601 acids (Gibco, #11130-036), 0.1 mg ml^{-1} proline, and 0.85 mg ml^{-1} Pluronic F127 (Sigma-Aldrich,
602 P2443), and the temperature was set to 37 °C.

603

604 **EdU pulse labelling**

605 Cells grown until A_{600} of ~0.1 were labelled with 10 μM EdU (5-Ethynyl-2´-deoxyuridine,
606 Thermofisher, C10337) for 15 min after which cells were washed, introduced to fresh media
607 containing 60 μg/ml thymidine and allowed to grow for 3 h. Following this, cells were fixed
608 with 4% PFA (v/v) for 30 min and permealized with 0.5% Triton X-100 (v/v) for 30 min. EdU
609 click-chemistry reaction was conducted following the instructions (Thermofisher, #C10337)
610 using Alexa 488 azide in a final volume of 50 μl for 30 min at room temperature, followed by
611 washing. Cells were then labelled with TMR HaloTag ligand as in (Banaz et al., 2019). Briefly,
612 cells were incubated with 2 μM TMR ligand for 30 min and washed several times. Finally,

613 nucleoids were labelled with 1 μg/ml DAPI for 15 min and washed, after which the cells were
614 ready for imaging.
615
616 **Epifluorescence microscopy**
617 Fluorescence images were acquired on an inverted fluorescence microscope (Ti-E, Nikon)
618 equipped with a perfect focus system, a 100× NA 1.4 oil immersion objective, a motorized
619 stage, an sCMOS camera (Orca Flash 4, Hamamatsu), and a temperature chamber (Okolabs).
620 Exposure times were 300 ms for TMR, Alexa 488 and mCherry, mYpet; 150 ms for mCerulean,
621 and 100 ms for DAPI using an LED excitation source (Lumencor SpectraX). Phase contrast
622 images were collected for cell segmentation. Microscopy data was collected automatically
623 from the sample area. Time-lapse images were collected every 10 min for 3 h with a shorter
624 exposure time of 150 ms, except fluorescence images from the microfluidics device were
625 collected every 5 min.
626
627 **Microfluidic devices**
628 The microfluidic single-cell imaging device ("mother machine") was prepared as in (Uphoff,
629 2018). The device was designed using Autodesk AutoCAD software. The dimensions of the
630 cell channels were 1.2 µm x 1.2 µm x 20 µm and the media flow channels were 100 µm x 25
631 µm. The structures were fabricated on a silicon wafer (Kavli Nanolab, Delft University)
632 (Moolman et al., 2013) and a negative polydimethylsiloxane (PDMS) mold was created from
633 the silicon wafer using a 5:1 mixture of monomer and curing agent (Dow Corning Sylgard
634 184 Kit). After removing air bubbles using vacuum, the chip was cured at 65°C for 1.5 hours.
635 The mould was treated with Trichloro(1H,1H,2H,2H perfluorooctyl)silane (Sigma) in vacuum
636 overnight. The PDMS device was generated from the negative mold using a 10:1 mixture of
637 monomer and curing agent and cured at 65°C for 1.5 hours. Media flow holes were punched
638 through the device with 0.75 mm diameter. Cover slips were cleaned by sonication in
639 acetone for 20 min, washing with dH2O, sonication in isopropanol for 20 min, and dried
640 with nitrogen. The PDMS device was washed with isopropanol and dried with nitrogen. The
641 device and a cover slip were bonded using air plasma (Plasma Etch PE-50) and placed in an
642 oven at 95°C for 30 min. Cells were pipetted into the device and the device was centrifuged
643 at 4000 rpm for 10 min to place cells into the channels. The media supplemented by
644 Pluronic F127 was fed into the device through silicon tubing (Tygon ND 100-80 microbore,
645 VWR) using a motorized infusion pump (New Era Pump Systems). Initially, a high flow rate of
646 1.5 ml/hr was applied to flush the excess cells and then lowered to 0.5 ml/hr. After this, cells
647 were allowed to grow for ~2 h before starting the time-lapse imaging.
648
649 **Image analysis**
650 Cell based information, including cell outlines, lineages, pole ages, per pixel fluorescence
651 intensities, and fluorescent marker localization, was extracted using SuperSegger (Stylianidou
652 et al., 2016) in MATLAB (MathWorks). SuperSegger uses an image-curvature method to
653 identify foci to avoid the identification of false positive foci due to background intensity from
654 cytoplasmic fluorescence and uses a gaussian fit to find the subpixel resolution location of
655 foci. Focus quality is determined by a combination of intensity and fitting parameters and bad
656 quality foci were filtered out. A threshold value was confirmed by visual inspection and the

657 same threshold was used for all compared data sets. The channels were aligned prior to
658 analysis.
659
660 *Mother machine analysis*
661 From the lineage data, cells were classified as 'normal' growing cells, anucleate cells, mothers
662 of anucleate cells and sisters of anucleate cells. Cells that disappeared early or didn't have a
663 tracked lineage were excluded from the analysis. Anucleate cells were considered as cells that
664 didn't divide, didn't elongate and lacked an *ori1* marker present, while its sister cell elongated
665 and divided normally, and had *ori1* marker(s). If neither of the sister cells divided normally,
666 cells were excluded from analysis. The older pole of the anucleate cell was traced back ≥2
667 generations to determine whether the anucleate cell formed on the older or newer pole of
668 the mother. The cell size at birth (Fig. S1B) was determined at the first frame of each cell and
669 the number of *ori1* foci prior to division (Fig. 1C) at the last frame of a cell.
670
671 *Fluorescent marker localization*
672 For *ori1, ter3, L3* and *R3* markers, intensity profiles with different cell lengths were
673 normalized, as the expectation is that a cell will have at least a single focus at all times. As
674 cell orientation is random relative to the pole age, cells were oriented to place *L3* more
675 towards the negative pole than *R3* and, in the *ori1* data, *ter3* was oriented more towards
676 the negative pole. To determine flipping frequency of *L3-R3-L3-R3* markers from time-lapse
677 imaging, first mother cells that contained at *L3-R3-L3-R3* or *R3-L3-R3-L3* were identified.
678 Next, their daughter cells with *L3-R3-L3-R3* or *R3-L3-R3-L3* were identified. The angle (Fig.
679 S2) between vectors pointing from the more polar *L3* to the more polar *R3* was calculated
680 between mother and daughter cells. If the angle exceeded 90°, the chromosome orientation
681 was considered flipped. To measure width of a unimodal distribution and to avoid
682 inaccuracy from binning the data, the data was fitted by a kernel distribution in MATLAB
683 and full width at half maximum (FWHM) was calculated from the fitted distribution.
684
685 *EdU pulse labelling*
686 A functional HaloTag fusion of the endogenous *tsr* gene was used in the EdU labeling, as click-
687 chemistry reaction conditions are detrimental to conventional fluorescent proteins. To
688 measure EdU association with the older pole, the following criteria were used to select cells
689 from an asynchronous cell population (see Fig. S4). First, Otsu's thresholding (Otsu, 1979) was
690 used to segment nucleoid area(s) from the cellular background and only cells that have two
691 separate, large-enough nucleoid areas were analysed. Second, a cell must exhibit a clear
692 difference in polar Tsr intensity. The center line of a cell was extracted to find coordinates of
693 cell poles by fitting a cell mask to a second-order curve. The intersection of the cell mask
694 border and the curve was used to define cell poles. Median Tsr intensity of the cell area was
695 subtracted from all Tsr pixel intensities and a sum of 9 brightest pixels from each pole were
696 used to quantify the pole intensity. To minimize effects of noise and discrete pixel size in
697 segmentation, only cells with >1.5-fold difference in polar Tsr intensity were analysed. The
698 pole that had a higher intensity of Tsr was designated as the older pole. Third, only one of the
699 nucleoids must be labelled by EdU. EdU with short incorporation times appear as distinct foci
700 (see Fig. 4 and Fig. S4). The foci below a fixed threshold for the score were discarded. The foci

were mapped to the nucleoids by projecting coordinates of both on the center line of the cell. With these criteria, the processed microscopy data from SuperSegger was automatically analysed to extract the result of EdU association with older cell pole. To avoid segmentation errors of the cell area, correct cell segmentation was visually inspected and inaccurately segmented cells were removed.

Tsr time-lapse

The accuracy of Tsr-based identification of the old cell pole in our growth conditions was estimated by tracking cells with a functional mYpet fusion to the endogenous *tsr* gene over generations under a microscope. Only cells that both were born and divided during the time-lapse were analysed. Tsr intensity at each pole was calculated with same criteria as in the EdU experiment. The accuracy of Tsr as the older pole marker was determined for each frame separately by comparing results between Tsr intensity analysis and lineage tracking. The accuracy (Fig. 4D) was shown for the last frame prior to division to mimic the EdU experiment where only cells with segregated chromosomes were analysed.

Acknowledgements

We thank other members of the Sherratt and Uphoff group, and Katarzyna Ginda-Mäkelä for insightful discussions. The research was supported by a Wellcome Investigator Award to DJS (200782/Z/16/Z). SU was in receipt of a Henry Dale-Wellcome Fellowship.

Author contributions

JM and DJS conceived the project and directed it. JM undertook and analyzed experiments. SU developed the microfluidics, advised on its use and was generally involved in project discussions. JM, SU and DJS wrote the paper.

Declaration of Interests

The authors declare no competing interests.

Data and code availability

All data required to understand and assess the conclusions of the research are available in the main text and supplementary materials. All materials and codes are available upon reasonable request.

735 **References**

736 Bachmann, B.J. (1996). Derivation and Genotypes of Some Mutant Derivatives of *Escherichia*
737 *coli* K-12. Escherichia Coli Salmonella Typhimurium Cell. Mol. Biol. *ASM*, 2460–2488.
738 Badrinarayanan, A., Reyes-Lamothe, R., Uphoff, S., Leake, M.C., and Sherratt, D.J. (2012). In
739 Vivo Architecture and Action of Bacterial Structural Maintenance of Chromosome Proteins.
740 Science *338*, 528–531.
741 Badrinarayanan, A., Le, T.B.K., and Laub, M.T. (2015). Bacterial Chromosome Organization
742 and Segregation. Annu. Rev. Cell Dev. Biol. *31*, 171–199.
743 Banaz, N., Mäkelä, J., and Uphoff, S. (2019). Choosing the right label for single-molecule
744 tracking in live bacteria: Side-by-side comparison of photoactivatable fluorescent protein
745 and Halo tag dyes. J. Phys. D. Appl. Phys. *52*, 064002.
746 Ben-Yehuda, S., Rudner, D.Z., and Losick, R. (2003). RacA, a bacterial protein that anchors
747 chromosomes to the cell poles. Science *299*, 532–536.
748 Bergmiller, T., Andersson, A.M.C., Tomasek, K., Balleza, E., Kiviet, D.J., Hauschild, R., Tkačik,
749 G., and Guet, C.C. (2017). Biased partitioning of the multidrug efflux pump AcrAB-TolC
750 underlies long-lived phenotypic heterogeneity. Science *356*, 311–315.
751 Brézellec, P., Hoebeke, M., Hiet, M.S., Pasek, S., and Ferat, J.L. (2006). DomainSieve: A
752 protein domain-based screen that led to the identification of dam-associated genes with
753 potential link to DNA maintenance. Bioinformatics *22*, 1935–1941.
754 Cairns, J. (1975). Mutation selection and the natural history of cancer. Nature *255*, 197–200.
755 Cass, J.A., Kuwada, N.J., Traxler, B., and Wiggins, P.A. (2016). *Escherichia coli* Chromosomal
756 Loci Segregate from Midcell with Universal Dynamics. Biophys. J. *110*, 2597–2609.
757 Danilova, O., Reyes-Lamothe, R., Pinskaya, M., Sherratt, D., and Possoz, C. (2007). MukB
758 colocalizes with the oriC region and is required for organization of the two *Escherichia coli*
759 chromosome arms into separate cell halves. Mol. Microbiol. *65*, 1485–1492.
760 Datsenko, K.A., and Wanner, B.L. (2000). One-step inactivation of chromosomal genes in
761 *Escherichia coli* K-12 using PCR products. Proc Natl Acad Sci U S A *97*, 6640– 6645.
762 David, A., Demarre, G., Muresan, L., Paly, E., Barre, F.X., and Possoz, C. (2014). The Two Cis-
763 Acting Sites, parS1 and oriC1, Contribute to the Longitudinal Organisation of *Vibrio cholerae*
764 Chromosome I. PLoS Genet. *10*, e1004448.
765 Davidson, I.F., Bauer, B., Goetz, D., Tang, W., Wutz, G., and Peters, J.-M. (2019). DNA loop
766 extrusion by human cohesin. Science *3418*, 1–13.
767 Ebersbach, G., Briegel, A., Jensen, G.J., and Jacobs-Wagner, C. (2008). A Self-Associating
768 Protein Critical for Chromosome Attachment, Division, and Polar Organization in
769 *Caulobacter*. Cell *134*, 956–968.
770 Errington, J., and Wake, R.G. (1991). Chromosome strand segregation during sporulation in
771 *Bacillus subtilis*. Mol. Microbiol. *5*, 1145–1149.
772 Espéli, O., Borne, R., Dupaigne, P., Thiel, A., Gigant, E., Mercier, R., and Boccard, F. (2012). A
773 MatP-divisome interaction coordinates chromosome segregation with cell division in *E. coli*.
774 EMBO J. *31*, 3198–3211.
775 Fisher, J.K., Bourniquel, A., Witz, G., Weiner, B., Prentiss, M., and Kleckner, N. (2013). Four-
776 Dimensional Imaging of *E. coli* Nucleoid Organization and Dynamics in Living Cells. Cell *153*,
777 882–895.
778 Fogel, M.A., and Waldor, M.K. (2005). Distinct segregation dynamics of the two *Vibrio*
779 *cholerae* chromosomes. Mol. Microbiol. *55*, 125–136.
780 Fritsche, M., Li, S., Heermann, D.W., and Wiggins, P.A. (2012). A model for *Escherichia coli*
781 chromosome packaging supports transcription factor-induced DNA domain formation.

782 Nucleic Acids Res. *40*, 972–980.
783 Ganji, A.M., Shaltiel, I.A., Bisht, S., Kim, E., Kalichava, A., Haering, C.H., and Dekker, C. (2018).
784 Real-time imaging of DNA loop extrusion by condensin. Science *7831*, 1–9.
785 Goloborodko, A., Imakaev, M. V., Marko, J.F., and Mirny, L. (2016). Compaction and
786 segregation of sister chromatids via active loop extrusion. Elife *5*, 1–16.
787 Hiraga, S., Niki, H., Ogura, T., Ichinose, C., Mori, H., Ezaki, B., and Jaffe, A. (1989).
788 Chromosome partitioning in *Escherichia coli*: novel mutants producing anucleate cells. J.
789 Bacteriol. *171*, 1496–1505.
790 Japaridze, A., Gogou, C., Kerssemakers, J.W.J., Nguyen, H.M., and Dekker, C. (2020). Direct
791 observation of independently moving replisomes in *Escherichia coli*. Nat. Commun. 3109.
792 Jun, S., and Mulder, B. (2006). Entropy-driven spatial organization of highly confined
793 polymers: lessons for the bacterial chromosome. Proc. Natl. Acad. Sci. U. S. A. *103*, 12388–
794 12393.
795 Kuzminov, A. (2014). The precarious prokaryotic chromosome. J. Bacteriol. *196*, 1793–1806.
796 Lansdorp, P.M. (2007). Immortal Strands? Give Me a Break. Cell *129*, 1244–1247.
797 Mäkelä, J., and Sherratt, D.J. (2020). Organization of the *Escherichia coli* Chromosome by a
798 MukBEF Axial Core. Mol. Cell *78*, 250–260.
799 Mangiameli, S.M., Veit, B.T., Merrikh, H., and Wiggins, P.A. (2017). The Replisomes Remain
800 Spatially Proximal throughout the Cell Cycle in Bacteria. PLOS Genet. *13*, e1006582.
801 Marczynski, G.T., Dingwall, A., and Shapiro, L. (1990). Plasmid and chromosomal DNA
802 replication and partitioning during the *Caulobacter crescentus* cell cycle. J. Mol. Biol. *212*,
803 709–722.
804 Marko, J.F., and Siggia, E.D. (1997). Polymer models of meiotic and mitotic chromosomes.
805 Mol. Biol. Cell *8*, 2217–2231.
806 McKenzie, G.J., and Craig, N.L. (2006). Fast, easy and efficient: Site-specific insertion of
807 transgenes into Enterobacterial chromosomes using Tn7 without need for selection of the
808 insertion event. BMC Microbiol. *6*, 39.
809 Mercier, R., Petit, M.A., Schbath, S., Robin, S., El Karoui, M., Boccard, F., and Espéli, O.
810 (2008). The MatP/*matS* Site-Specific System Organizes the Terminus Region of the *E. coli*
811 Chromosome into a Macrodomain. Cell *135*, 475–485.
812 Monterroso, B., Zorrilla, S., Sobrinos-Sanguino, M., Robles-Ramos, M.Á., Alfonso, C.,
813 Söderström, B., Meiresonne, N.Y., Verheul, J., Den Blaauwen, T., and Rivas, G. (2019). The
814 bacterial DNA binding protein matp involved in linking the nucleoid terminal domain to the
815 divisome at midcell interacts with lipid membranes. MBio *10*, 1–14.
816 Moolman, M.C., Huang, Z., Krishnan, S.T., Kerssemakers, J.W.J., and Dekker, N.H. (2013).
817 Electron beam fabrication of a microfluidic device for studying submicron-scale bacteria. J.
818 Nanobiotechnology *11*, 12.
819 Moolman, M.C., Krishnan, S.T., Kerssemakers, J.W., van den Berg, A., Tulinski, P., Depken,
820 M., Reyes-Lamothe, R., Sherratt, D.J., and Dekker, N.H. (2014). Slow unloading leads to DNA-
821 bound beta2-sliding clamp accumulation in live *Escherichia coli* cells. Nat Commun *5*, 5820.
822 Nielsen, H.J., Ottesen, J.R., Youngren, B., Austin, S.J., and Hansen, F.G. (2006). The
823 *Escherichia coli* chromosome is organized with the left and right chromosome arms in
824 separate cell halves. Mol. Microbiol *62*, 331–338.
825 Niki, H., and Jaffe, A. (1991). The new gene mukB codes for a 177 kd protein with coiled coil
826 domains involved in chromosome partitioning of *E. coli*. EMBO J. *10*, 183–193.
827 Nolivos, S., and Sherratt, D. (2014). The bacterial chromosome: Architecture and action of
828 bacterial SMC and SMC-like complexes. FEMS Microbiol. Rev. *38*, 380–392.

829 Nolivos, S., Upton, A.L., Badrinarayanan, A., Müller, J., Zawadzka, K., Wiktor, J., Gill, A.,
830 Arciszewska, L., Nicolas, E., and Sherratt, D. (2016). MatP regulates the coordinated action
831 of topoisomerase IV and MukBEF in chromosome segregation. Nat. Commun. *7*, 10466.
832 Nolivos, S., Cayron, J., Dedieu, A., Page, A., Delolme, F., and Lesterlin, C. (2019). Role of
833 AcrAB-TolC multidrug efflux pump in drug-resistance acquisition by plasmid transfer.
834 Science *364*, 778–782.
835 Osley, M.A., and Newton, A. (1974). Chromosome segregation and development in
836 Caulobacter crescentus. J. Mol. Biol. *90*, 359–370.
837 Otsu, N. (1979). A threshold selection method from gray-level histograms. IEEE Trans. Sys.
838 Man. Cyber. *9*, 62–66.
839 Ozaki, S., Matsuda, Y., Keyamura, K., Kawakami, H., Noguchi, Y., Kasho, K., Nagata, K.,
840 Masuda, T., Sakiyama, Y., and Katayama, T. (2013). A replicase clamp-binding dynamin-like
841 protein promotes colocalization of nascent DNA strands and equipartitioning of
842 chromosomes in *E.coli*. Cell Rep. *4*, 985–995.
843 Petrushenko, Z.M., She, W., and Rybenkov, V. V. (2011). A new family of bacterial
844 condensins. Mol. Microbiol. *81*, 881–896.
845 Ping, L., Weiner, B., and Kleckner, N. (2008). Tsr-GFP accumulates linearly with time at cell
846 poles, and can be used to differentiate “old” versus “new” poles, in *Escherichia coli*. Mol.
847 Microbiol. *69*, 1427–1438.
848 Rando, T.A. (2007). The Immortal Strand Hypothesis: Segregation and Reconstruction. Cell
849 *129*, 1239–1243.
850 Reyes-Lamothe, R., Possoz, C., Danilova, O., and Sherratt, D.J. (2008). Independent
851 Positioning and Action of *Escherichia coli* Replisomes in Live Cells. Cell *133*, 90–102.
852 Soubry, N., Wang, A., and Reyes-Lamothe, R. (2019). Replisome activity slowdown after
853 exposure to ultraviolet light in *Escherichia coli*. Proc. Natl. Acad. Sci. U. S. A. *116*, 11747–
854 11753.
855 Stylianidou, S., Brennan, C., Nissen, S.B., Kuwada, N.J., and Wiggins, P.A. (2016).
856 SuperSegger: robust image segmentation, analysis and lineage tracking of bacterial cells.
857 Mol. Microbiol. *102*, 690–700.
858 Surovtsev, I. V., and Jacobs-Wagner, C. (2018). Subcellular Organization: A Critical Feature of
859 Bacterial Cell Replication. Cell *172*, 1271–1293.
860 Toro, E., and Shapiro, L. (2010). Bacterial Chromosome Organization and Segregation. Cold
861 Spring Harb Perspect Biol *2*, a000349.
862 Uhlmann, F. (2016). SMC complexes: From DNA to chromosomes. Nat. Rev. Mol. Cell Biol.
863 *17*, 399–412.
864 Umbarger, M.A., Toro, E., Wright, M.A., Porreca, G.J., Baù, D., Hong, S.H., Fero, M.J., Zhu,
865 L.J., Marti-Renom, M.A., McAdams, H.H., et al. (2011). The three-dimensional architecture
866 of a bacterial genome and its alteration by genetic perturbation. Mol. Cell *44*, 252–264.
867 Uphoff, S. (2018). Real-time dynamics of mutagenesis reveal the chronology of DNA repair
868 and damage tolerance responses in single cells. Proc. Natl. Acad. Sci. U. S. A. *115*, E6516–
869 E6525.
870 Vallet-Gely, I., and Boccard, F. (2013). Chromosomal Organization and Segregation in
871 *Pseudomonas aeruginosa*. PLoS Genet. *9*, e1003492.
872 Wakeman, J.A., Hmadcha, A., Soria, B., and McFarlane, R.J. (2012). The immortal strand
873 hypothesis: Still non-randomly segregating opinions. Biomol. Concepts *3*, 203–211.
874 Waldminghaus, T., and Skarstad, K. (2009). The *Escherichia coli* SeqA protein. Plasmid *61*,
875 141–150.

Wallden, M., Fange, D., Lundius, E.G., Baltekin, O., and Elf, J. (2016). The Synchronization of Replication and Division Cycles in Individual *E. coli* Cells. Cell *166*, 729–739.
Wang, P., Robert, L., Pelletier, J., Dang, W.L., Taddei, F., Wright, A., and Jun, S. (2010). Robust growth of *Escherichia coli*. Curr. Biol. *20*, 1099–1103.
Wang, X., Possoz, C., and Sherratt, D.J. (2005). Dancing around the divisome: asymmetric chromosome segregation in *Escherichia coli*. Genes Dev *19*, 2367–2377.
Wang, X., Liu, X., Possoz, C., and Sherratt, D.J. (2006). The two *Escherichia coli* chromosome arms locate to separate cell halves. Genes Dev. *20*, 1727–1731.
Wang, X., Reyes-lamothe, R., and Sherratt, D.J. (2008). Modulation of *Escherichia coli* sister chromosome cohesion by topoisomerase. Genes Dev. 2426–2433.
Wang, X., Llopis, P.M., and Rudner, D.Z. (2013). Organization and segregation of bacterial chromosomes. Nat. Rev. Genet. *14*, 191–203.
Wang, X., Montero Llopis, P., and Rudner, D.Z. (2014). *Bacillus subtilis* chromosome organization oscillates between two distinct patterns. Proc. Natl. Acad. Sci. U. S. A. *2014*, 1–6.
White, M.A., Eykelenboom, J.K., Lopez-Vernaza, M.A., Wilson, E., and Leach, D.R.F. (2008). Non-random segregation of sister chromosomes in *Escherichia coli*. Nature *455*, 1248–1250.
Wu, L.J., and Errington, J. (2003). RacA and the Soj-Spo0J system combine to effect polar chromosome segregation in sporulating *Bacillus subtilis*. Mol. Microbiol. *49*, 1463–1475.
Wu, F., Japaridze, A., Zheng, X., Wiktor, J., Kerssemakers, J.W.J., and Dekker, C. (2019). Direct imaging of the circular chromosome in a live bacterium. Nat. Commun. *10*, 1–9.
Yamaichi, Y., Bruckner, R., Ringgaard, S., Möll, A., Ewen Cameron, D., Briegel, A., Jensen, G.J., Davis, B.M., and Waldor, M.K. (2012). A multidomain hub anchors the chromosome segregation and chemotactic machinery to the bacterial pole. Genes Dev. *26*, 2348–2360.
Yang, S., Kim, S., Kim, D.K., Jeon An, H., Bae Son, J., Hedén Gynnå, A., and Ki Lee, N. (2019). Transcription and translation contribute to gene locus relocation to the nucleoid periphery in E. coli. Nat. Commun. *10*, 1–12.
Zawadzki, P., Stracy, M., Ginda, K., Zawadzka, K., Lesterlin, C., Kapanidis, A.N., and Sherratt, D.J. (2015). The Localization and Action of Topoisomerase IV in *Escherichia coli* Chromosome Segregation Is Coordinated by the SMC Complex, MukBEF. Cell Rep. *13*, 2587–2596.

Supplementary Figures

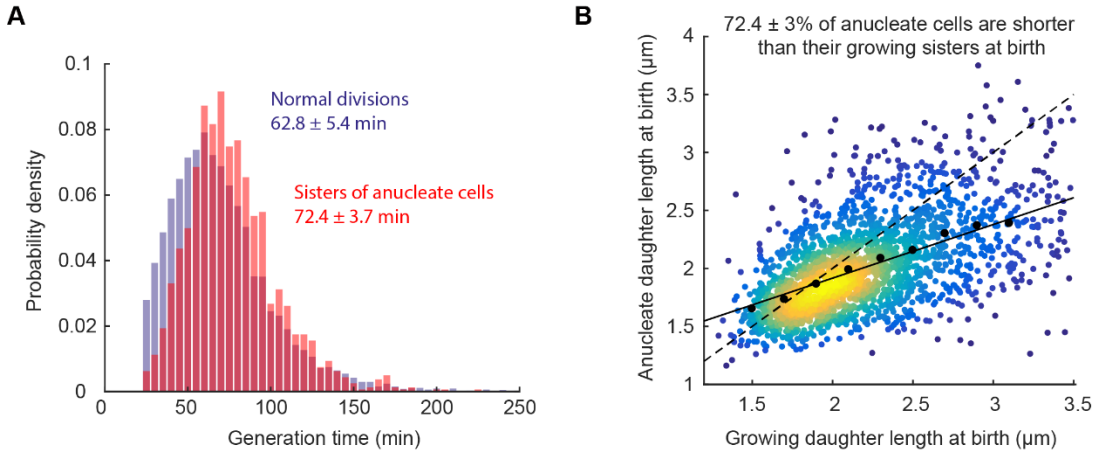

Fig. S1. (**A**) Generation time in normally dividing cells (12103 cells) and in sisters of anucleate cells (1605 cells). Two-sample t-test of mean generation time p-value 0.2176. Data from 3 repeats. (**B**) Difference in cell length at birth between anucleate and growing sister cells at anucleate cell division. Black dashed line indicates symmetric division and solid line shows a linear fit to the data. Black circles show binned mean. 2266 cell pairs from 3 repeats.

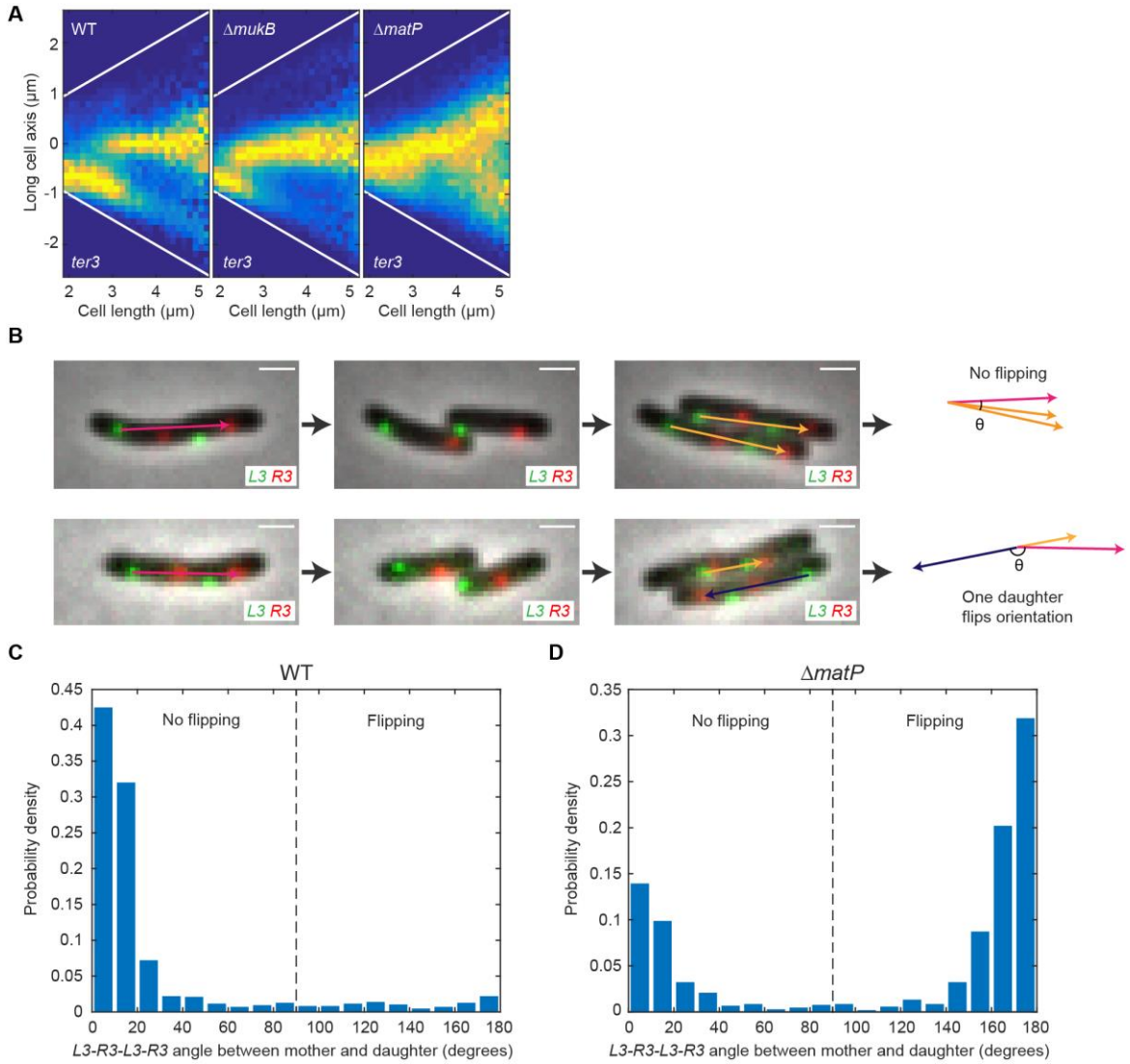

Fig. S2. (**A**) *ter3* localization along long cell axis in WT (26926 cells), Δ*mukB* (48770 cells) and Δ*matP* (45532 cells). From same data as in Fig. 2D; *ter3* is oriented more towards the negative pole than *ori1*. Data from 3 repeats. (**B**) Representative time-lapse images of WT (top) and *ΔmatP* (bottom) cells with *L3* and *R3* markers. (top) *L3-R3-L3-R3* orientation is maintained over a generation while (bottom) *L3-R3-L3-R3* orientation is flipped. From *L3-R3-L3-R3* cells, angle between vectors pointing from the more polar *L3* to the more polar *R3* is calculated between mother cell (red arrow) and daughter cells (orange arrow) and, if the angle exceeds 90°, the chromosome orientation is considered flipped (blue arrow). Scale bars: 1 μm. Angle between mother and daughter cell *L3-R3-L3-R3* vectors in (**C**) WT (859 pairs) and (**D**) *ΔmatP* (1054 pairs) cells. Data from 3 repeats.

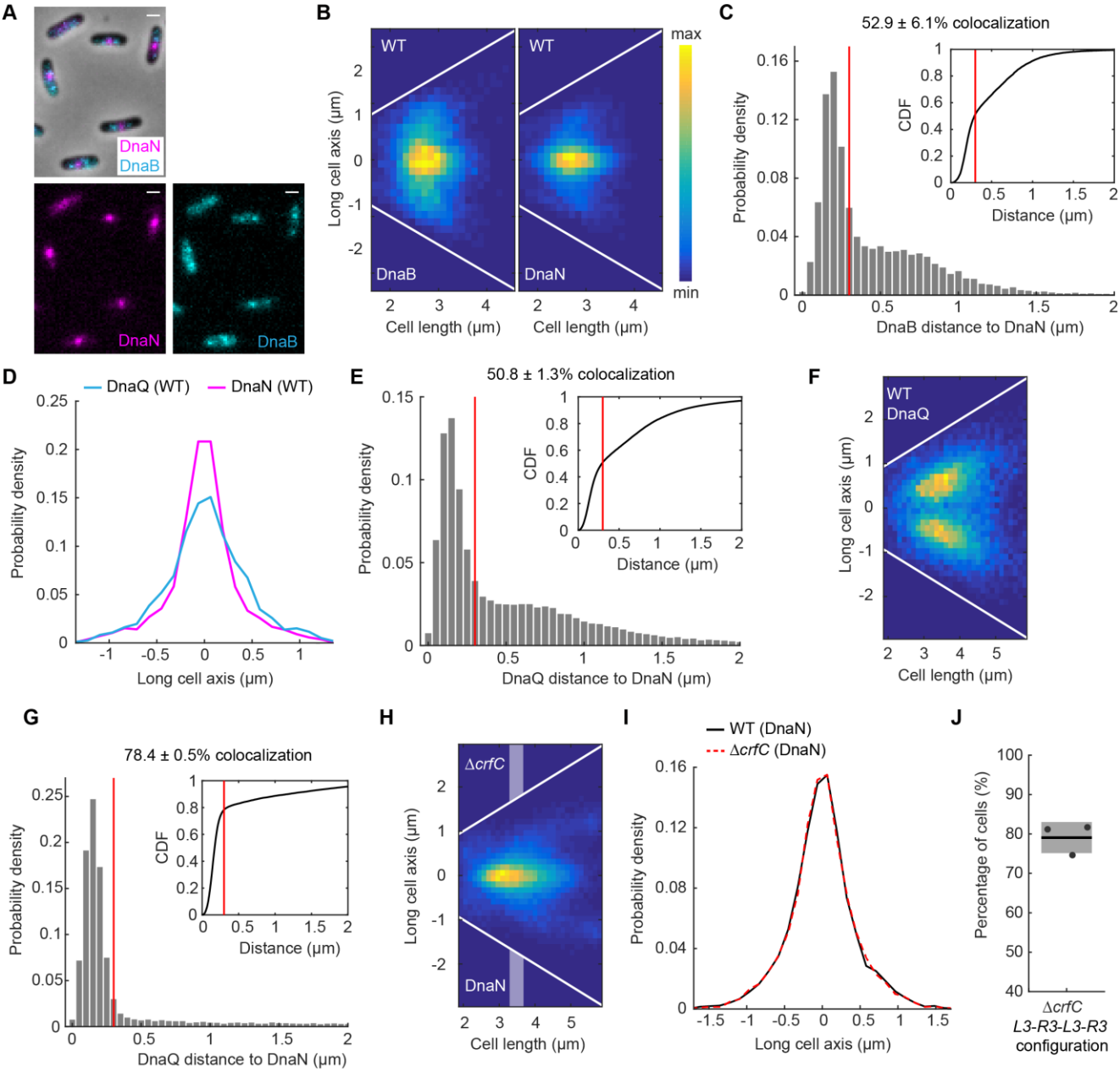

Fig. S3. (**A**) Representative images of WT cells with labelled DnaN and DnaB. Scale bars: 1 μm. (**B**) DnaB and DnaN localization in WT cells as a function of cell length (16134 cells). White lines denote cell borders. (**C**) Distance from a DnaB locus to the closest DnaN locus. DnaB and DnaN colocalize in 52.9 ± 6.1% (±SD) of pairs (11714 pairs) as defined by a threshold (red lines) below which two proteins colocalize (dictated by a diffraction limit of 300 nm). Inset shows the same data as a cumulative distribution. Same data as in (B). (**D**) DnaQ (4567 spots) or DnaN (5393 spots) localization with early replication cells in WT (cell lengths 2.5-2.9 μm) (same data as in Fig. 3C). (**E**) Distance from a DnaQ locus to the closest DnaN locus in *ΔmatP* cells. DnaQ and DnaN colocalize in 50.8 ± 1.3% (±SD) of pairs (46330 pairs). Inset shows the same data as a cumulative distribution. Same data as in (Fig. 3F). (**F**) DnaQ localization as a function of cell length in WT cells in which DnaQ foci are spatially separate from DnaN (16158 cells). Same data as in Fig. 2C and D. (**G**) Distance from a DnaQ locus to the closest DnaN locus in *ΔmukB* cells. DnaQ and DnaN colocalize in 78.4 ± 0.5%

941 (±SD) of pairs (32603 pairs). Inset shows the same data as a cumulative distribution. Same
942 data as in (Fig. 3G). (**H**) DnaN localization in *ΔcrfC* cells as a function of cell length (49955
943 cells). Shaded areas denote intermediate cell lengths for localization data in (I). White lines
944 denote cell borders. (**I**) DnaN localization with intermediate cell lengths (3.3-3.7 µm) in WT
945 (8006 spots) and *ΔcrfC* (10691). Data from (H) and Fig. 3E. (**J**) Percentage of *ΔcrfC* cells (8393
946 cells) with *L3-R3-L3-R3* (or *R3-L3-R3-L3*) configuration (versus *L3-R3-R3-L3* or *R3-L3-L3-R3*) in
947 double *L3* and *R3* focus cells. All data from 3 repeats.
948

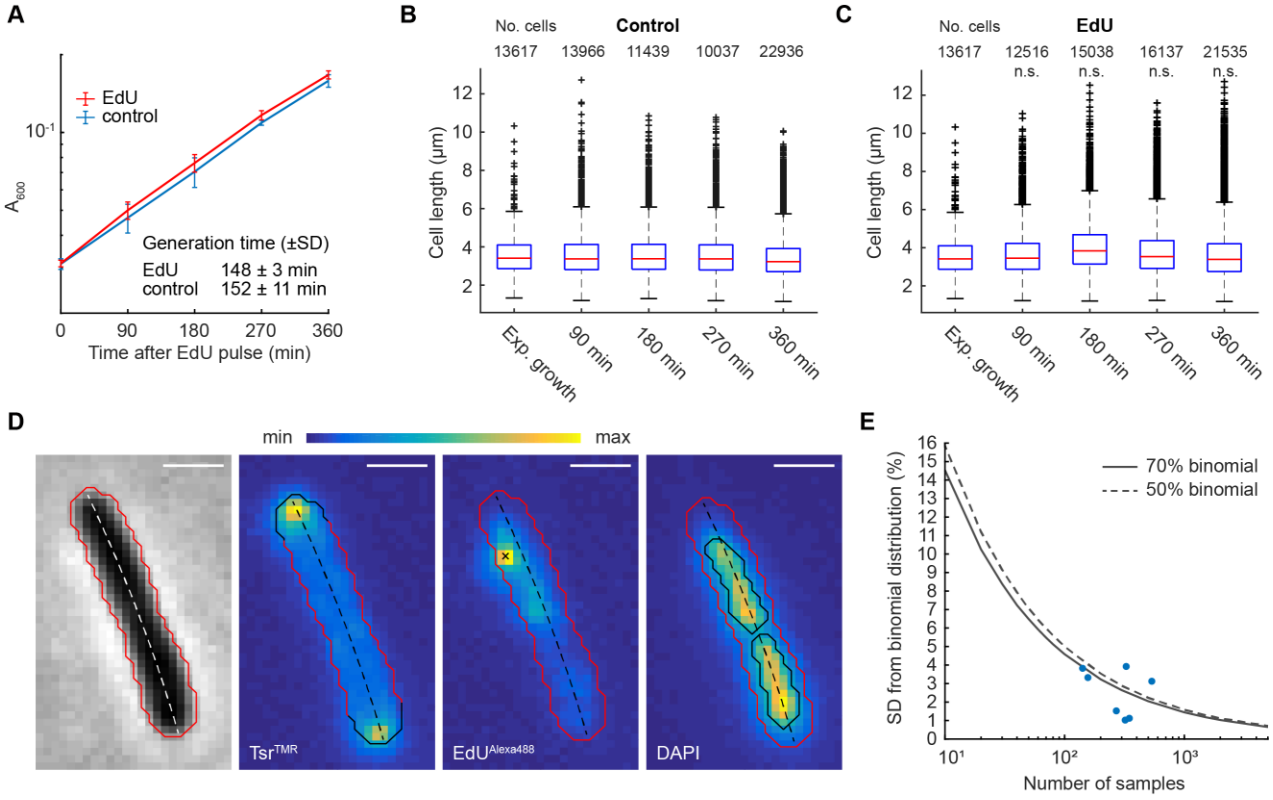

Fig. S4. (**A**) Cell growth following a 15 min EdU pulse compared to no EdU. Cell length at different time intervals (**B**) without or (**C**) with EdU pulse. n.s. indicates two-sample t-test of mean cell length compared to control p-value > 0.01. Data from 3 repeats. (**D**) Image analysis of EdU experiment. A representative cell after EdU protocol showing Tsr^{TMR}, EdU^{Alexa488} and DAPI labelling. Red line is the cell border and dashed line shows the center line of the cell. Black line in Tsr^{TMR} channel shows the pole areas from where the Tsr intensity is calculated. Black cross in EdU^{Alexa488} channel indicates a detected EdU focus. Black lines in DAPI channel indicate segmented nucleoid areas. For more information see Methods. Scale bars: 1 µm (**E**) Accuracy of the retention measurement as function of sample size. Different sample sizes were drawn from a binomial distribution with 50% (dashed line) or 70% (solid line) success rate and SD was calculated between them (10^5 repeats for each value). The data from Fig. 5 are shown with dots.

964 **Table S1.** Strain list.

Strain	Relevant genotype	Source or reference
AB1157	F^-, λ^-, rac^-, *thi-1, hisG4, Δ(gpt-proA)62, argE3, thr-1, leuB6, kdgK51, rfbD1, araC14, lacY1, galK2, xylA5, mtl-1, tsx-33, supE44(glnV44), rpsL31*(str^R), qsr'-0, mgl-51	Coli Genetic Stock Center (CGSC) #1157 (Bachmann, 1996)
AU2101	AB1157, *lacO*240 at *ori1* (3908) (*hyg*), *tetO*240 at *ter3* (1644) (*gen*), *ΔleuB::Plac-lacI-mCherry-frt, ΔgalK::Plac-tetR-mCerulean-frt, ΔmukB::kan*	(Nolivos et al., 2016)
JM09	AB1157, *lacO*240 at *ori1* (3908) (*hyg*), *tetO*240 at *ter3* (1644) (*gen*), *ΔleuB::Plac-lacI-mCherry-frt, ΔgalK::Plac-tetR-mCerulean-frt, attTn7-GFPmut2, Δflhd-frt, ΔmukB::kan*	This study
JM122	AB1157, *tsr-HaloTag-kan*	This study
JM127	AB1157, *tsr-HaloTag-frt*, *ΔmatP::kan*	This study
JM128	AB1157, *tsr-HaloTag-frt*, *ΔseqA::kan*	This study
JM130	AB1157, *tsr-HaloTag-frt*, *Δdam::kan*	This study
JM131	AB1157, *tsr-HaloTag-frt*, *ΔmukB::kan*	This study
JM133	AB1157, *tsr-mYpet-kan*	This study
JM135	AB1157, *lacO240 at L3 (2268) (hyg), tetO240 at R3 (852) (gen), ΔleuB::Plac-lacI-mCherry-frt, ΔgalK::Plac-tetR-mCerulean-frt, ΔmatP::kan*	This study
JM136	AB1157, *tsr-HaloTag-frt*, *matPΔC20-kan*	This study
JM137	AB1157, *tsr-HaloTag-frt*, *ΔzapB::kan*	This study
JM140	AB1157, *lacO240 at L3 (2268) (hyg), tetO240 at R3 (852) (gen), ΔleuB::Plac-lacI-mCherry-frt, ΔgalK::Plac-tetR-mCerulean-frt, ΔmukB::kan*	This study
JM141	AB1157, *frt-mCherry-dnaN, dnaQ-Ypet-kan*	This study
JM142	AB1157, *frt-mcherry-dnaN, ΔyjdA::kan*	This study
JM143	AB1157, *lacO240 at L3 (2268) (hyg), tetO240 at R3 (852) (gen), ΔleuB::Plac-lacI-mCherry-frt, ΔgalK::Plac-tetR-mCerulean-frt, ΔyjdA::kan*	This study
JM150	AB1157, *frt-mCherry-dnaN, dnaQ-Ypet-frt, ΔmatP::kan*	This study
JM152	AB1157, *frt-mCherry-dnaN, dnaQ-Ypet-frt, ΔmukB::kan*	This study
JW4070	*ΔyjdA::kan*	Coli Genetic Stock Center (CGSC) #10929
RRL36	AB1157, *dnaQ-Ypet-kan*	(Reyes-Lamothe et al., 2008)
RRL66	AB1157, *lacO240 at L3 (2268) (hyg), tetO240 at R3 (852) (gen), ΔleuB::Plac-lacI-mCherry-frt, ΔgalK::Plac-tetR-mCerulean-frt*	(Reyes-Lamothe et al., 2008)

RRL189	AB1157, *lacO*240 at *ori1* (3908) (*hyg*), *tetO*240 at *ter3* (1644) (*gen*), Δ*leuB::Plac-lacI-mCherry-frt, ΔgalK::Plac-tetR-mCerulean-frt*	(Reyes-Lamothe et al., 2008)
RRL388	AB1157, *frt-mCherry-dnaN*	(Soubry et al., 2019)
RRL396	AB1157, *frt-Ypet-dnaB, kan-mCherry-dnaN*	(Soubry et al., 2019)
SN192	AB1157, *lacO*240 at *ori1* (3908) (*hyg*), *tetO*240 at *ter3* (1644) (*gen*), Δ*leuB::Plac-lacI-mCherry-frt, ΔgalK::Plac-tetR-mCerulean-frt, mukB-mYpet-frt*	(Nolivos et al., 2016)
SN302	AB1157, *lacO*240 at *ori1* (3908) (*hyg*), *tetO*240 at *ter3* (1644) (*gen*), Δ*leuB::Plac-lacI-mCherry-frt, ΔgalK::Plac-tetR-mCerulean-frt, mukB-mYpet-frt, ΔmatP::cat*	(Nolivos et al., 2016)

Table S2. Primer list

Name	**Sequence**	**Construct**
JMP48_Fw	CGCCGCGTAAAATGGCCGTGGCAGATAGCGAGGAGAACTGGGAAACATTTTCGGCTGGCTCCGCTGC	λ-red attachment of *HaloTag-kan* or *mYpet-kan* to *tsr* at the endogenous locus.
JMP49_Rv	AATCTCCTTATGCCCGATAACATTTTGCTTATCGGGCATTTTCATGGCGATATGAATATCCTCCTTAGTTCCTAT	